

**Accelerated Article Preview**

# Hidden states and dynamics of fractional fillings in twisted MoTe<sub>2</sub> bilayers

---

Received: 8 September 2024

Accepted: 28 March 2025

---

Accelerated Article Preview

Published online: 03 April 2025

---

Cite this article as: Wang, Y. et al.

Hidden states and dynamics of fractional fillings in twisted MoTe<sub>2</sub> bilayers. *Nature*  
<https://doi.org/10.1038/s41586-025-08954-8>  
(2025)

---

Yiping Wang, Jeongheon Choe, Eric Anderson, Weijie Li, Julian Ingham, Eric A. Arsenault, Yiliu Li, Xiaodong Hu, Takashi Taniguchi, Kenji Watanabe, Xavier Roy, Dmitri Basov, Di Xiao, Raquel Queiroz, James C. Hone, Xiaodong Xu & X.-Y. Zhu

---

This is a PDF file of a peer-reviewed paper that has been accepted for publication. Although unedited, the content has been subjected to preliminary formatting. Nature is providing this early version of the typeset paper as a service to our authors and readers. The text and figures will undergo copyediting and a proof review before the paper is published in its final form. Please note that during the production process errors may be discovered which could affect the content, and all legal disclaimers apply.

## Hidden states and dynamics of fractional fillings in twisted MoTe<sub>2</sub> bilayers

Yiping Wang<sup>1,2</sup>, Jeongheon Choe<sup>1</sup>, Eric Anderson<sup>3</sup>, Weijie Li<sup>3</sup>, Julian Ingham<sup>4</sup>, Eric A. Arsenault<sup>1</sup>, Yiliu Li<sup>1</sup>, Xiaodong Hu<sup>5</sup>, Takashi Taniguchi<sup>6</sup>, Kenji Watanabe<sup>7</sup>, Xavier Roy<sup>1</sup>, Dmitri Basov<sup>4</sup>, Di Xiao<sup>5</sup>, Raquel Queiroz<sup>4</sup>, James C. Hone<sup>2</sup>, Xiaodong Xu<sup>3,5</sup>, X.-Y. Zhu<sup>1,\*</sup>

<sup>1</sup> Department of Chemistry, Columbia University, New York, NY 10027, USA

<sup>2</sup> Department of Mechanical Engineering, Columbia University, New York, NY 10027, USA

<sup>3</sup>Department of Physics, University of Washington, Seattle, WA 98195, USA

<sup>4</sup>Department of Physics, Columbia University, New York, NY 10027, USA

<sup>5</sup> Department of Materials Science and Engineering, University of Washington, Seattle, WA 98195, USA

<sup>6</sup>Research Center for Materials Nanoarchitectonics, National Institute for Materials Science, 1-1 Namiki, Tsukuba 305-0044, Japan

<sup>7</sup> Research Center for Electronic and Optical Materials, National Institute for Materials Science

1-1 Namiki, Tsukuba 305-0044, Japan

<sup>7</sup> Research Center for Electronic and Optical Materials, National Institute for Materials Science, 1-1 Namiki, Tsukuba 305-0044, Japan

The fractional quantum anomalous Hall (FQAH) effect was recently discovered in twisted MoTe<sub>2</sub> bilayers (tMoTe<sub>2</sub>)<sup>1-4</sup>. Experiments to date have revealed Chern insulators from hole doping at  $\nu = -1, -2/3, -3/5$ , and  $-4/7$  (per moiré unit cell)<sup>1-6</sup>. In parallel, theories predict that, between  $\nu = -1$  and  $-3$ , there exist exotic quantum phases<sup>7-15</sup>, such as the coveted fractional topological insulators (FTI), fractional quantum spin Hall (FQSH) states, and non-abelian fractional states. Here we employ transient optical spectroscopy<sup>16,17</sup> on tMoTe<sub>2</sub> to reveal nearly 20 hidden states at fractional fillings that are absent in static optical sensing or transport measurements. A pump pulse selectively excites charge across the correlated or pseudo gaps, leading to the disordering (melting) of correlated states<sup>18</sup>. A probe pulse detects the subsequent melting and recovery dynamics via exciton and trion sensing<sup>1,3,19-21</sup>. Besides the known states, we observe additional fractional fillings between  $\nu = 0$  and  $-1$  and a large number of states on the electron doping side ( $\nu > 0$ ). Most importantly, we observe new states at fractional fillings of the Chern bands at  $\nu = -4/3, -3/2, -5/3, -7/3, -5/2$ , and  $-8/3$ . These states

\* To whom correspondence should be addressed. E-mail: xyzhu@columbia.edu.

32 **are potential candidates for the predicted exotic topological phases<sup>7-15</sup>. Moreover, we show**  
33 **that melting of correlated states occurs on two distinct time scales, 2-4 ps and 180-270 ps,**  
34 **attributed to electronic and phonon mechanisms, respectively. We discuss the differing**  
35 **dynamics of the electron and hole doped states from the distinct moiré conduction and**  
36 **valence bands.**

37       Quantum states that support fractional charge excitations are fascinating manifestations of  
38 many-body interactions in condensed matter. These states, originally discovered as the fractional  
39 quantum Hall (FQH) effect in 2D electron gases at high magnetic fields<sup>22</sup>, have been observed  
40 recently in moiré superlattices of tMoTe<sub>2</sub> bilayers<sup>1-4</sup> and multilayer graphene/hexagonal boron-  
41 nitride interfaces<sup>23</sup> in the absence of magnetic field. Unlike fractional charge orderings from  
42 generalized Wigner crystal formation in moiré bands<sup>20,21,24,25</sup>, the recently discovered FQAH  
43 effects<sup>1-4,23</sup> represent fractional charge excitations obeying anyon statistics, formed from many  
44 body correlations in flat Chern bands. In addition to the FQAH states, fractional fillings between  
45  $\nu = -1$  and  $-3$  have been predicted to result in other exotic quantum phases<sup>7-15</sup>, but these states  
46 have not been detected to date. A transport measurement assigned a  $\nu = -3$  state to FQSH state<sup>26</sup>,  
47 but the presence of ferromagnetic order may challenge this interpretation<sup>27,28</sup>.

48       To find new states in the Chern bands, we investigate dual-gated R-stacked MoTe<sub>2</sub> bilayers  
49 with twist angles of  $\theta = 3.7^\circ$  and  $3.1^\circ$ , respectively (Fig. 1a, detailed in Extended Data Fig. 1),  
50 known to exhibit FQAH effects<sup>1-4</sup>. In our approach<sup>16,17</sup>, illustrated in Fig. 1b for a Mott insulator,  
51 a pump pulse with  $\hbar\omega_1$  (0.99 eV) below the optical gap (1.12 eV)<sup>1</sup> of MoTe<sub>2</sub> induces intraband  
52 excitation of a doped electron or hole. Relaxation within the continuum of conduction or valence  
53 band states occurs on ultrafast ( $\leq 100$  fs) time scales (II)<sup>16,17,29</sup>, but the correlation gap provides a  
54 bottleneck in relaxation and leads to the transient formation of excitation across the gap (III),  
55 referred to as a holon-doublon pair in a Mott insulator<sup>18</sup>. The presence of sufficient excitation  
56 leads to disordering and gap-closing<sup>16-18</sup> (IV), followed by recovery at longer times (V). This  
57 approach also applies to correlated electron liquid, where the bottleneck in intraband relaxation  
58 leads to the transient formation of excitation across a pseudo-gap, thus disrupting correlation and  
59 renders the system more Fermi liquid like. The dynamics are followed as a function of pump-probe  
60 delay ( $\Delta t$ ) from exciton ( $\sim 1.120$ -1.135 eV) and trion ( $\sim 1.100$ -1.120 eV) sensing by the probe pulse  
61 ( $\hbar\omega_2$ ), which detects the increase in the effective dielectric constant and the resulting decrease in

oscillator strengths<sup>19–21</sup>. We present  $\Delta R/R$ , where  $\Delta R = R(\Delta t) - R$ ;  $R(\Delta t)$  and  $R$  are the reflectance spectrum at  $\Delta t$  and before time zero (static), respectively. The pump-induced change is detected as a reduced amplitude of the derivative-shaped resonance and  $\Delta R/R$  shows a characteristic flip in sign from that of  $R$  (Fig. 1c). Our measurement reveals predominantly the equilibrium states before they are “melted” by the pump pulse. We do not observe increases in oscillator strength after photo-excitation, indicating transient formation of correlated insulators are not important. The sensitivity and specificity of pump-probe spectroscopy comes from its background-free nature, because the correlated states are selectively perturbed by the pump pulse when the photon energy is below the optical gaps of constituent 2D semiconductors.

## Time domain detection of fractional fillings of the Chern bands: $\theta = 3.7^\circ$

We first focus on sample D1 ( $\theta = 3.7^\circ$ ) and compare the static reflectance spectrum (Fig. 1d) and transient spectra, Fig. 1e and 1f at  $\Delta t = 13$  ps and 300 ps, respectively, as functions of gate voltage ( $V_g$ ) and  $\hbar\omega_2$ . In static spectrum, the  $v = -1$  and 1 states can be identified by the enhancements in  $R$ . The transient spectra show drastically enhanced resolution and sensitivity, leading to the detection of 20 states. Fig. 1g shows selected linecuts at exciton (black) and trion (orange) resonances, with the moiré filling factor  $v$  listed (see Method and Extended Data Table 1). A static spectroscopic technique based a separate WSe<sub>2</sub> sensor layer was used to detect a large number of correlated insulators in the topologically trivial WS<sub>2</sub>/WSe<sub>2</sub> moiré superlattice<sup>21</sup>, but this approach is less sensitive for the tMoTe<sub>2</sub> system<sup>3</sup>.

On the electron side, we resolve  $v = 1$  and at least 10 states at fractional fillings. The number of states identified here is more than twice of those detected in steady-state spectroscopic sensing<sup>1</sup>. These states, also observed in other transition metal dichalcogenide (TMD) moiré systems, have been called generalized Wigner crystals<sup>20,21,24,25</sup>. They are formed when the onsite ( $U$ ) and inter-site ( $V$ ) Coulomb energies overwhelm the kinetic energy ( $t$ ). In WS<sub>2</sub>/WSe<sub>2</sub> moiré superlattices, Arsenault et al. recently pointed out the similarity of generalized Wigner crystals to charge density waves (CDW) and showed evidences for the polaronic nature of localized charges<sup>16</sup>.

From hole doping of the Chern bands, we observe states at  $v = -1, -2/3, -1/2, -1/3$ , and likely  $-3/5$  and  $-2/5$ . These states have been predicted in the phase diagrams for hole doping<sup>30</sup>. The  $v = -1, -2/3, -3/5$  states are zero-field Chern insulators<sup>1–4</sup> and  $v = -1/2$  a composite Fermi-liquid<sup>31</sup>. The

v = -1/3 state is in the region without magnetic order and is a topologically trivial charge order state<sup>8,30,32</sup>. The v = -2/5 state is also in the non-magnetic region<sup>28</sup> and possibly a charge order state. For doping beyond v = -1, we observe new fractional states at v = -4/3, -3/2, and -5/3. Each of these new states exhibits a small feature on top of intense  $\Delta R/R$  signal over broad doping levels (v < -1.2). Since transport measurements showed no gaps in this doping range<sup>26-28</sup>, we assign the broad background  $\Delta R/R$  to the disruption of highly correlated liquid states from pump excitation across pseudo gaps. Thus, the observed v = -4/3, -3/2, and -5/3 states are likely incipient, emerging from the highly correlated liquid states.

While the above experiments are carried out at a sample temperature of 2.0 K, we also perform temperature-dependent measurements (Extended Data Fig. 2). On the electron side, many of the charge order states exist at T = 7 K, with v = 1 persisting to T = 20 K. On the hole side, the v = -4/3, -3/2, and -5/3 states are no longer resolved at elevated temperatures, but there is evidence for pump-induced reduction in oscillator strength persisting to T ≥ 7 K. The v = -1 state can be resolved at early pump-probe delays at T = 20 K, which is higher than the critical temperature of  $T_c \sim 13$  K reported earlier<sup>1,2</sup>. These findings suggest that our transient measurement is sensitive to not only correlated insulators but also to residual electronic correlations above nominal  $T_c$ .

## Time domain detection of fractional fillings of the Chern bands: $\theta = 3.1^\circ$

We carry out transient measurements on a second tMoTe<sub>2</sub> sample (D2) with  $\theta = 3.1^\circ$ . While the competition between kinetic energy and Coulomb energies varies with  $\theta$ , band topologies of tMoTe<sub>2</sub> are unchanged for the two twist angles ( $\theta = 3.1^\circ$  and  $3.7^\circ$ )<sup>33-35</sup>. Fig. 2a and Fig. 2b show  $\Delta R/R$  maps at representative delays,  $\Delta t = 13$  ps and 450 ps, respectively. The lower moiré unit cell density of D2 compared to D1 allows us to reach filling factors close to v = ±3. While the abundant charge ordered states on the electron side remain clearly observed, those from the hole side are harder to resolve. To improve resolution, we present 2D spectral maps in derivative form,  $d(\Delta R/R)/dn$ , where n is the doping density ( $\propto V_g$ ). Fig. 2c show  $d(\Delta R/R)/dn$  spectral maps averaged over  $\Delta t = 13$ , 25, and 45 ps; each state is identified at the inflection point connecting a peak and a valley. Fig. 2d shows selected line-cuts at  $\Delta t = 13$  ps and 450 ps. States at v ≥ -1 are resolved in both time windows, while those between v = -1 and -3 are only observed at  $\Delta t = 13$  ps, not at  $\Delta t = 450$  ps. The three states at v = -4/3, -3/2, and -5/3 observed in D1 are reproduced in D2. Between

120  $v = -2$  and  $-3$ , we resolve three new states at  $v = -8/3, -5/2$ , and  $-7/3$ . As in D1, the  $v = -4/3, -3/2, -$   
121  $5/3, -8/3, -5/2$ , and  $-7/3$  states in D2 all exhibit small features on top of intense and broad  $\Delta R/R$   
122 signal. These states are likely incipient from highly correlated liquids with pseudo gaps. In addition  
123 to the new states at  $v < -1$ , we observe a series of fractional states at  $v = -1/5, -1/3, -1/2, -2/3, -4/5$ .  
124 Overall, we resolve a total of 29 states.

125 **Control Sample at  $\theta = 5.5^\circ$**

126 As a control to the above findings of correlated states at  $\theta = 3.7^\circ$  and  $3.1^\circ$ , we carry out  
127 measurements on a tMoTe<sub>2</sub> sample with a larger twist angle of  $\theta = 5.5^\circ$  (D3), Extended data Fig.  
128 3. No correlated states have been found at such a large twist angle<sup>1-4</sup> and we confirm this in  
129 doping-dependent photoluminescence (PL) measurement. Consistent with static PL sensing, no  
130 states are detected in pump-probe spectral mapping in the entire doping range ( $-5.5 \times 10^{12}$  to  
131  $5.5 \times 10^{12} \text{ cm}^{-2}$ ).

132 **Melting dynamics: electronic vs. phononic**

133 Having identified a zoo of states, we now investigate their melting and reordering dynamics.  
134 We present  $\Delta R/R$  maps at  $\Delta t = 1.5 - 300 \text{ ps}$ , Fig. 3 for D1. Similar spectral maps for D2 are shown  
135 in Extended Data Fig. 4. The correlated states are observed in the entire time window, with varying  
136 degrees of resolution. On the electron side, there are two distinct time windows of melting and  
137 recovery, as evidenced by the  $\Delta R/R$  signal reaching the first minimum between 1.5 and 13 ps.  
138 Following partial recovery,  $\Delta R/R$  decreases again on the longer time scale of  $\sim 300 \text{ ps}$ , before  
139 recovering on ns time scales (see Fig. 4 for time-traces). On the hole side, we observe primarily  
140 the first melting characterized by a minimum at  $\Delta t \sim 13 \text{ ps}$ .

141 To understand the origins of melting/recovery processes, we present in Fig. 4 selected temporal  
142 profiles for D1 at (a)  $v = \pm 1$ , (b)  $v = \pm 4/3$ , (c)  $v = \pm 3/2$ , (d)  $v = 0$  at the probe photon energy where  
143  $\Delta R/R$  reaches minimum. Similar profiles for other filling factors are summarized in Extended  
144 Data Fig. 5. For electron doping, the time profiles are characterized by initial decays with time  
145 constants of  $\tau_{m1} = 2-3.5 \text{ ps}$  and recoveries with time constants of  $\tau_{r1} = 20 - 40 \text{ ps}$ . This stage  
146 following excitation can be attributed to disordering from charge hopping<sup>16-18</sup> and we call this  
147 “electronic melting”. As control, we confirm that this fast melting/recovery process is absent for  
148  $v = 0$ , Fig. 4d, where only the decaying tail of an initial spike is observed; the latter likely originates

149 from transient response of the graphite gates (See Method)<sup>16,17</sup>. In sample D2, there are clearly  
150 resolved states near  $V_g = 0$ , making the precise assignment of charge neutrality difficult (see  
151 Methods). The state closest to  $V_g = 0$  (arrow in Fig. 2b or 2e) is likely a hole-doped state at  $-1/7 \leq$   
152  $v < 0$ . Confirming this, we show that the electronic melting process is observed at 2 K but  
153 disappears at 70 K ( $> T_c$ ), Extended Data Fig. 6. At this low doping level, electronic melting and  
154 recovery occur with time constants of  $\tau_{m1} = 1.5 \pm 0.5$  ps and  $\tau_{r1} = 3.4 \pm 0.9$  ps, respectively, both  
155 shorter than corresponding time constants at higher hole doping levels.

156 For  $v = 0, 1, 4/3$ , and  $3/2$ , we observe at  $\Delta\tau > 7$  ps high frequency oscillations that are known  
157 coherent phonon wavepackets launched at the graphite electrodes by the excitation pulse and  
158 arrived at tMoTe<sub>2</sub> with a time delay (Extended Data Fig. 7)<sup>36,37</sup>. For  $v = 0$ , we find that the  
159 excitation of phonons in tMoTe<sub>2</sub> decreases the oscillator strengths of both excitons and trions  
160 (Extended Data, Fig. 8), as shown by  $\Delta R/R$  reaching a minimum at  $\Delta t = 300 \pm 20$  ps, Fig. 4d.  
161 However, this change alone does not explain the observations at  $v = 1, 4/3$ , and  $3/2$  (Fig. 4a-c), as  
162 their magnitudes in the decrease of  $\Delta R/R$  are much larger than that at  $v = 0$ . Moreover, the  
163 occurrences of the second minima for  $v = 1, 4/3$ , and  $3/2$  are time delayed from that of  $v = 0$  by  
164 ~150 ps, likely reflecting the time for re-heating the electrons by phonons. Thus, the second  
165 minima in  $\Delta R/R$  observed for  $v = 1, 4/3$ , and  $3/2$  reveal an additional mechanism for pump-induced  
166 increases in effective dielectric constants specific of the correlated states, i.e, re-melting of these  
167 states. We refer to this stage as “phonon melting”, similar to strain wave induced melting of CDW  
168 and semiconductor-to-metal transitions<sup>38,39</sup>. The phonon melting is responsible for the much-  
169 enhanced contrast in transient spectra for some of the correlated states at long time delays, Fig. 1  
170 and Fig. 2.

171 We now turn to the melting and recovery dynamics of states at  $v = -1, -4/3$ , and  $-3/2$ . While  
172 the  $v = -1$  state is well-resolved, the  $v = -4/3$  and  $-3/2$  states are identified only as weak features  
173 on a broad continuum. These states are likely incipient, emerging from a highly correlated liquid  
174 with pseudo gaps. The time profiles at  $v = -4/3$  and  $-3/2$  probe predominantly the dynamics of the  
175 underlying correlated liquid. The most obvious difference from electron doping is that phonon  
176 oscillations and the subsequent phonon melting/recovery are much reduced for hole doping at  $v =$   
177  $-1$ , and becomes negligible for  $v = -4/3$  and  $-3/2$ . The negligible phonon perturbation for  $v = -1$  is  
178 associated with an absence of spectral changes in exciton and trion sensing, in contrast to a time-

179 dependent blue shift observed for the phonon-perturbed  $v = 1$  state, Extended Data, Fig. 8.  
180 Moreover, the electronic melting processes of states from hole doping are slower than those of  
181 corresponding electron doping (Fig. 4a-c). The melting and recovery time constants for  $v = -1$ , -  
182 4/3, and -3/2 are  $\tau_{m1} = 4.3\text{-}6.5$  ps and  $\tau_{r1} = 24\text{-}38$  ps, respectively.

183 Here we present a tentative interpretation, Fig. 4f. The key feature of twisted TMD bilayers  
184 is the layer skyrmion texture of interlayer tunneling<sup>33</sup>. There are three distinct stacking regions  
185 at small twist angles – AA, XM, and MX. Interlayer tunneling is large in the AA regions but  
186 vanishes in the MX/XM regions. For electron doping, the moiré conduction band derive  
187 primarily from the  $Q$  point due to interlayer hybridization<sup>32,40</sup> and are delocalized  
188 spatially in zigzag stripes across the entire moiré unit cell<sup>40</sup>. This results in a large  
189 energy oscillation ( $\delta_{ph}$ ) by the breathing phonon, which modulates the interlayer  
190 distance and, thus, hybridization. The hybridized and spatially delocalized nature also  
191 facilitates inter-site hopping ( $t_h$ ) of holons and doublons, thus, accelerating melting  
192 and recovery dynamics. In contrast, for hole doped states ( $v < 0$ ), the uppermost moiré  
193 valence band near the  $K$  points is localized to the MX or XM regions that form the honeycomb  
194 lattice<sup>33–35</sup>. The layer localized and nonbonding nature suggests that hole-doped states are  
195 insensitive to interlayer distance, leading to small  $\delta_{ph}$ . Holon/doublon hopping is inhibited  
196 between neighboring MX/XM sites and is also small between next-nearest neighbor sites, thus  
197 slowing melting and recovery dynamics. In the presence of large displacement field, the hole  
198 doped states are polarized to a single layer<sup>1–4</sup>; Holon/doublon hopping  $t_h$  may be increased and  
199 the modulation of displacement field by the breathing mode may also increase the magnitude  
200 of  $\delta_{ph}$ , as are observed in Fig 4e.

201 While the qualitative proposal based on spatial wavefunction variations provides a tentative  
202 explanation of the differing dynamics of electron and hole doped states, theories are needed to  
203 quantitative understand these differences. Moreover, the honeycomb MX/XM lattice is also related  
204 to the formation of topological states; whether the robustness of some of the hole doped states as  
205 compared to the electron doped ones is related to topology remains an open question.

206 **Discussions**

Our results establish the presence of the  $v = -4/3, -3/2, -5/3, -7/3, -5/2$ , and  $-8/3$  states from fractional fillings of the Chern bands in tMoTe<sub>2</sub>. The discovery of these states that have evaded detection in prior experiments <sup>1–4,26,27,41</sup> underscores the superior sensitivity of our time-domain approach. These states are located in the phase space with small or no ferromagnetic order <sup>27,28</sup>. While their origins cannot be confirmed here, some of these fractional states are candidates for the exotic topological states predicted in recent theories <sup>7–15</sup>. Kwan et al. <sup>7</sup> proposed the  $v = -4/3$  state potentially as an abelian FTI consisting of two copies of  $v = -2/3$  in the K and K' valleys, stabilized by phonon coupling and/or sufficient nonlocal Coulomb screening. Chen et al. <sup>42</sup> suggested  $v = -3/2$  as a non-abelian FCI, but the lack of spin/valley polarization<sup>27</sup> argues against this proposal. May-Mann et al. <sup>11</sup> proposed half-integer FQSH edge states to form pairs of charged counter-propagating bosonic modes; our observed  $v = -3/2$  and  $-5/2$  states might be related to these proposed edges states. We are not aware of theories on the  $v = -5/3$  and  $-7/3$  states; an intriguing possibility is that they are FCIs, but fluctuations of weak magnetic order may make experimental verification difficult. The  $v = -8/3$  state is weakly magnetic<sup>27</sup> and potentially a topological state in the second moiré band. Further theoretical studies are warranted.

An intriguing question is why states at  $v = -4/3, -3/2, -5/3, -7/3, -5/2$ , and  $-8/3$  have not been resolved in prior transport measurements, that showed no evidence of gap formation at these fillings<sup>26–28</sup>. These states are likely incipient, emerging from highly correlated liquid states in the broad doping range ( $-3 < v < -1.2$ ). While the pump-probe approach can be sensitive to remanent correlation and pseudo gaps, transport measurements are not. Improved transport measurements are needed to isolate the correlated insulator responses from interfering effects of liquid-like states. One may also fully develop the correlated gaps from incipient states by sample engineering, e.g., reduction in disorder and control of dielectric screening, to allow the detection of quantized transport, particularly with edge resolution.

231

## 232 **References**

- 233 1. Cai, J. *et al.* Signatures of fractional quantum anomalous Hall states in twisted MoTe<sub>2</sub>.  
234 *Nature* **622**, 63–68 (2023).
- 235 2. Park, H. *et al.* Observation of fractionally quantized anomalous Hall effect. *Nature* **622**,  
236 74–79 (2023).
- 237 3. Zeng, Y. *et al.* Thermodynamic evidence of fractional Chern insulator in moiré MoTe<sub>2</sub>.  
238 *Nature* **622**, 69–73 (2023).

- 239 4. Xu, F. *et al.* Observation of integer and fractional quantum anomalous Hall effects in  
240 twisted bilayer MoTe 2. *Phys Rev X* **13**, 031037 (2023).
- 241 5. Ji, Z. *et al.* Local probe of bulk and edge states in a fractional Chern insulator. *Nature* **635**,  
242 578–583 (2024).
- 243 6. Redekop, E. *et al.* Direct magnetic imaging of fractional Chern insulators in twisted  
244 MoTe2. *Nature* **635**, 584–589 (2024).
- 245 7. Kwan, Y. H. *et al.* When Could Abelian Fractional Topological Insulators Exist in  
246 Twisted MoTe2 (and Other Systems). *arXiv preprint arXiv:2407.02560* (2024).
- 247 8. Yu, J. *et al.* Fractional Chern insulators versus nonmagnetic states in twisted bilayer MoTe  
248 2. *Phys Rev B* **109**, 045147 (2024).
- 249 9. Zhang, Y.-H. Vortex spin liquid with neutral Fermi surface and fractional quantum spin  
250 Hall effect at odd integer filling of moiré Chern band. *arXiv preprint arXiv:2402.05112*  
251 (2024).
- 252 10. Wang, C. *et al.* Higher Landau-Level Analogues and Signatures of Non-Abelian States in  
253 Twisted Bilayer MoTe 2. *arXiv preprint arXiv:2404.05697* (2024).
- 254 11. May-Mann, J., Stern, A. & Devakul, T. Theory of half-integer fractional quantum spin  
255 Hall insulator edges. *arXiv preprint arXiv:2403.03964* (2024).
- 256 12. Sodemann Villadiego, I. Halperin states of particles and holes in ideal time reversal  
257 invariant pairs of Chern bands and the fractional quantum spin Hall effect in moiré MoTe  
258 2. *Phys Rev B* **110**, 045114 (2024).
- 259 13. Xu, C., Mao, N., Zeng, T. & Zhang, Y. Multiple Chern bands in twisted MoTe 2 and  
260 possible non-Abelian states. *arXiv preprint arXiv:2403.17003* (2024).
- 261 14. Reddy, A. P., Paul, N., Abouelkomsan, A. & Fu, L. Non-Abelian fractionalization in  
262 topological minibands. *arXiv preprint arXiv:2403.00059* (2024).
- 263 15. Ahn, C.-E., Lee, W., Yananose, K., Kim, Y. & Cho, G. Y. First Landau Level Physics in  
264 Second Moiré Band of Twisted Bilayer MoTe 2. *arXiv preprint arXiv:2403.19155* (2024).
- 265 16. Arseneault, E. A. *et al.* Two-Dimensional Moiré Polaronic Electron Crystals. *Phys Rev Lett*  
266 **132**, 126501 (2024).
- 267 17. Arseneault, E. A. *et al.* Time-Domain Signatures of Distinct Correlated Insulators in a  
268 Moiré Superlattice. *arXiv preprint arXiv:2406.15067* **16**, 549 (2024).
- 269 18. Murakami, Y., Golež, D., Eckstein, M. & Werner, P. Photo-induced nonequilibrium states  
270 in Mott insulators. *arXiv preprint arXiv:2310.05201* (2023).
- 271 19. Tang, Y. *et al.* Simulation of Hubbard model physics in WSe<sub>2</sub>/WS<sub>2</sub> moiré superlattices.  
272 *Nature* **579**, 353–358 (2020).
- 273 20. Regan, E. C. *et al.* Mott and generalized Wigner crystal states in WSe<sub>2</sub>/WS<sub>2</sub> moiré  
274 superlattices. *Nature* **579**, 359–363 (2020).
- 275 21. Xu, Y. *et al.* Correlated insulating states at fractional fillings of moiré superlattices.  
276 *Nature* **587**, 214–218 (2020).
- 277 22. Stormer, H. L., Tsui, D. C. & Gossard, A. C. The fractional quantum Hall effect. *Rev Mod  
278 Phys* **71**, S298 (1999).
- 279 23. Lu, Z. *et al.* Fractional quantum anomalous Hall effect in multilayer graphene. *Nature*  
280 **626**, 759–764 (2024).
- 281 24. Li, H. *et al.* Imaging two-dimensional generalized Wigner crystals. *Nature* **597**, 650–654  
282 (2021).
- 283

- 284 25. Li, H. *et al.* Wigner molecular crystals from multielectron moiré artificial atoms. *Science*  
285 (1979) **385**, 86–91 (2024).
- 286 26. Kang, K. *et al.* Evidence of the fractional quantum spin Hall effect in moiré MoTe2.  
287 *Nature* **628**, 522–526 (2024).
- 288 27. Park, H. *et al.* Ferromagnetism and Topology of the Higher Flat Band in a Fractional  
289 Chern Insulator. *arXiv preprint arXiv:2406.09591* (2024).
- 290 28. Anderson, E. *et al.* Programming correlated magnetic states with gate-controlled moiré  
291 geometry. *Science* (1979) **381**, 325–330 (2023).
- 292 29. Petek, H. & Ogawa, S. Femtosecond time-resolved two-photon photoemission studies of  
293 electron dynamics in metals. *Prog Surf Sci* **56**, 239–310 (1997).
- 294 30. Reddy, A. P. & Fu, L. Toward a global phase diagram of the fractional quantum  
295 anomalous Hall effect. *Phys Rev B* **108**, 245159 (2023).
- 296 31. Anderson, E. *et al.* Trion sensing of a zero-field composite Fermi liquid. *Nature* **635**, 590–  
297 595 (2024).
- 298 32. Wang, C. *et al.* Fractional chern insulator in twisted bilayer mote2 (2023). *Phys Rev Lett*  
299 **132**, 036501 (2024).
- 300 33. Wu, F., Lovorn, T., Tutuc, E., Martin, I. & MacDonald, A. H. Topological insulators in  
301 twisted transition metal dichalcogenide homobilayers. *Phys Rev Lett* **122**, 086402 (2019).
- 302 34. Zhang, X.-W. *et al.* Polarization-driven band topology evolution in twisted MoTe2 and  
303 WSe2. *Nat Commun* **15**, 4223 (2024).
- 304 35. Abouelkomsan, A., Reddy, A. P., Fu, L. & Bergholtz, E. J. Band mixing in the quantum  
305 anomalous Hall regime of twisted semiconductor bilayers. *Phys Rev B* **109**, L121107  
306 (2024).
- 307 36. Yoon, Y. *et al.* Terahertz phonon engineering with van der Waals heterostructures. *Nature*  
308 **631**, 771–776 (2024).
- 309 37. Li, Y. *et al.* Coherent Modulation of Two-Dimensional Moiré States with On-Chip THz  
310 Waves. *Nano Lett* **24**, 12156–12162 (2024).
- 311 38. Amano, T. *et al.* Propagation of insulator-to-metal transition driven by photoinduced  
312 strain waves in a Mott material. *Nat Phys* 1–8 (2024).
- 313 39. Mariette, C. *et al.* Strain wave pathway to semiconductor-to-metal transition revealed by  
314 time-resolved X-ray powder diffraction. *Nat Commun* **12**, 1239 (2021).
- 315 40. Magorrian, S. J. *et al.* Multifaceted moiré superlattice physics in twisted WSe 2 bilayers.  
316 *Phys Rev B* **104**, 125440 (2021).
- 317 41. Xu, F. *et al.* Interplay between topology and correlations in the second moiré band of  
318 twisted bilayer MoTe2. *arXiv preprint arXiv:2406.09687* (2024).
- 319 42. Chen, F., Luo, W.-W., Zhu, W. & Sheng, D. N. Robust non-Abelian even-denominator  
320 fractional Chern insulator in twisted bilayer MoTe  $\$ _2\$$ . *arXiv preprint arXiv:2405.08386* (2024).

325 **Figure 1. Pump-probe spectroscopy detects hidden states at fractional fillings in tMoTe<sub>2</sub>.** **a.**  
326 Schematics of a dual-gated MoTe<sub>2</sub> bilayer device (D1) with a twist angle  $\theta = 3.7^\circ$ . The pump photon energy  
327 is  $\hbar\omega_1=0.99$  eV and the broadband probe photo energies  $\hbar\omega_2 = 1.0\text{-}1.2$  eV. **b.** Schematic illustration of  
328 pump-induced processes in a correlated state, illustrated here for a Mott state with a lower and upper  
329 Hubbard band (LHB and UHB). Excitation creates hot carriers that relax on ultrafast time scales (II) to  
330 form a holon-doublon pair across the gap (III). These are followed by disordering/melting as represented  
331 by a reduction or closing of the correlated gap (IV), followed by recovery on a longer time scale (V). **c.**  
332 Schematic illustration of an exciton or trion reflection spectrum from a correlated state, with change induced  
333 by the pump and the corresponding differential reflectance spectrum. **d.** Static reflection spectrum ( $R$ ) as a  
334 function of gate bias ( $V_g$ ) and probe photon energy ( $\hbar\omega_2$ ). **e. & f.** Transient reflection spectra,  $\Delta R/R$  (pseudo  
335 color), where  $\Delta R = R(\Delta t) - R$ , as a function of  $V_g$  and  $\hbar\omega_2$  for delay times of  $\Delta t = 13$  ps and 300 ps,  
336 respectively. **g.** Linecuts from the spectral maps **f** at exciton (black) and trion (red) energies. The calibrated  
337 filling factors ( $v$ ) are indicated on the line cuts. All experiments carried are out at a sample temperature of  
338  $T = 2.0$  K.  
339  
340

341 **Figure 2. Pump-probe spectroscopy detects hidden states at fractional fillings of the first and second**  
342 **Chern bands in tMOTe<sub>2</sub> device 2 (D2) with a twist angle  $\theta = 3.1^\circ$ .** Transient reflection spectra,  $\Delta R/R$   
343 (pseudo color), where  $\Delta R = R(\Delta t) - R$ , as a function of  $V_g$  and  $\hbar\omega_2$  for delay times of  $\Delta t = 13$  ps (**a**) and 450  
344 ps (**b**), respectively. Panels (**c**) is a derivative spectral map  $d(\Delta R/R)/dV_g$ , averaged over three early delays  
345 times ( $\Delta t = 13, 25$ , and 45 ps). The color scales are normalized, negative (blue) to positive (red). (**d**) Linecuts  
346 from the spectral maps of  $\Delta R/R$  at exciton (black or grey), trion (red) energies, and from derivative spectral  
347 map  $d(\Delta R/R)/dn$ . The calibrated filling factors ( $v$ ) are indicated on the line cuts.). All experiments carried  
348 are out at a sample temperature of  $T = 2.0$  K.  
349

350 **Figure 3. Melting and recovery dynamics of correlated states.** Transient reflection spectra at the  
351 indicated pump-probe delay times (from top to bottom) of  $\Delta t = 1.5, 13, 25, 37, 49, 150, 300$  ps for **a.** hole  
352 doping and **b.** electron doping. The arrows illustrate the time windows for electronic melting/reordering  
353 and phonon melting/reordering. All spectra obtained from Device D1 ( $\theta = 3.7^\circ$ ), at a sample temperature of  
354  $T = 2.0$  K.  
355

356 **Figure 4. Melting and recovery dynamics.** Time profiles of transient reflection ( $\Delta R/R$ ) for: **a**  $v = \pm 1$ , **b**  
357  $v = \pm 4/3$ , **c**  $v = \pm 3/2$ , and **d**  $v = 0$  from device D1 ( $\theta = 3.7^\circ$ ). **e.** Time profiles of the  $v = -1$  state in device  
358 D2 ( $\theta = 3.1^\circ$ ) at two displacement fields,  $D = 0.0$  (red) and 0.2 V/nm (blue). Each profile is obtained at the  
359 probe photon energy where  $\Delta R/R$  reaches minimum, integrated over a small spectral window ( $\pm 2$  meV).  
360 Note that each panel is divided into two scales (0-75 ps and 75 – 1875 ps). In panels **a**, **b**, **c**, and **e**, the  $\Delta R/R$   
361 values are normalized to the minima on the short time scale (< 20 ps). In panel **d**, there is no minimum on  
362 the short time scale (< 20 s) and the normalization factor was an average of those in panels **a-c**. The  
363 normalized  $\Delta R/R$  values between 75-1875 ps in panels **a**, **b**, and **c** are scaled by a factor of 0.5. All data  
364 obtained at a sample temperature of  $T = 2.0$  K with zero displacement field. **f.** Illustration of the moiré  
365 superlattice showing the layer-localized and non-bonding XM/MX (blue/orange) regions that form the  
366 honeycomb lattice, and the interlayer hybridized AA regions. The lower panel illustrates inter-site hopping  
367 ( $t_h$ ) and modulation of electronic states by the breathing phonon ( $\delta_{ph}$ ) in the conduction band (CB) and  
368 valence band (VB).  
369  
370

371 **METHODS**372 **Device Fabrication and Doping**

373 Flakes of the van der Waals materials used to fabricate the heterostructure devices – graphite,  
374 h-BN, and monolayer MoTe<sub>2</sub> – were mechanically exfoliated onto oxygen-plasma cleaned Si/SiO<sub>2</sub>  
375 substrates and identified by optical contrast under an optical microscope. Atomic force microscopy  
376 (AFM) was used to determine h-BN thickness and confirm the flakes to be free of residue. As  
377 MoTe<sub>2</sub> was air sensitive, its exfoliation, as well as the rest of the device fabrication process, was  
378 performed in an argon filled glovebox with H<sub>2</sub>O and O<sub>2</sub> concentrations less than 0.1 ppm. Before  
379 starting the transfer, the MoTe<sub>2</sub> monolayer was cut in half by an AFM tip. Standard dry transfer  
380 techniques were used to fabricate the heterostructure. First, the top gate was formed by picking up  
381 h-BN, the top graphite flake, the top gate h-BN dielectric, and a graphite grounding pin. Next, the  
382 first half of the MoTe<sub>2</sub> flake was picked up, the other half was rotated by the desired angle, and  
383 then picked up and placed down to form the moiré superlattice. Finally, the stack was placed down  
384 on a prepared backgate. This backgate consisted of an h-BN dielectric layer on top of a graphite  
385 flake, as well as gold contacts and wire bonding pads deposited using standard electron beam  
386 lithography and E-beam evaporation, allowing for electrical contact to both gates and to the  
387 grounding pin. The back gate was AFM-cleaned in contact mode before use. The finished  
388 heterostructure was placed onto the SiO<sub>2</sub>/Si substrate (SiO<sub>2</sub> thickness: 285 nm for D1 and 90 nm  
389 for D2) by melting down the PC at ~170 °C, and the stamp polymer was dissolved in anhydrous  
390 chloroform in a glovebox environment for 5 minutes, completing the device. For D1, the top and  
391 bottom h-BN gate dielectrics are both 35nm. For D2, the top gate h-BN is 32nm and the bottom  
392 gate h-BN is 37nm. We estimate the thickness of graphite electrodes from optical contrast on the  
393 Si/SiO<sub>2</sub> substrate. For D1, the top gate graphite is approximately 2-3 graphene layers, and the  
394 bottom is ~10 nm. For D2, the top is approximately two graphene layers and bottom ~2-3 nm.

395 **Determination of carrier density and twist angle**

396 The thickness of the bottom hBN layer in the tMoTe<sub>2</sub> devices was measured by an atomic  
397 force microscopy (AFM). We calculated the geometrical capacitance per unit area between the  
398 gate and the sample using the formula  $C_g = \frac{\epsilon_{hBN}\epsilon_0}{d_{hBN}}$ , where  $\epsilon_{hBN}=3.0$  is the dielectric constant of h-  
399 BN<sup>1,2</sup>,  $\epsilon_0$  is the vacuum permittivity,  $d_{hBN}$  is the thickness of the top or bottom h-BN layer. This  
400 equation applies to either side of tMoTe<sub>2</sub> sample to give top ( $C_{tg}$ ) or bottom ( $C_{bg}$ ) capacitance. The

401 carrier density in tMoTe<sub>2</sub> was determined by  $n = (V_{tg}C_{tg} + V_{bg}C_{bg})/e$ , where  $V_{tg/bg}$  is the top/bottom  
402 gate voltage, and  $e$  is the elementary charge. The twist angles of the tMoTe<sub>2</sub> were determined from  
403 the spectral features observed in reflectance contrast measurements. The exciton resonance in  
404 tMoTe<sub>2</sub> shows abrupt changes at superlattice filling factors  $\nu = \pm 1$  (Fig. 1 and Fig. 2), enabling us  
405 to extract the corresponding carrier density. The twist angle was calculated from  $\theta = \sqrt{3}/2 \cdot a_0 \cdot$   
406  $180/\pi$ , where  $a_0 = 3.52$  Å is the MoTe<sub>2</sub> lattice constant.

#### 407 **Reflection contrast measurements**

408 Each tMoTe<sub>2</sub> sample was mounted in a closed-cycle cryostat (Quantum Design, OptiCool) for  
409 all experiments, with a base temperature of 1.97 K during experiments. Steady-state reflectance  
410 measurements were carried out using a broadband lamp (Thorlabs, SLS201L). To minimize  
411 heating, a 1100 nm ±50 nm band-pass filter and a neutral density filter were employed. After  
412 collimation, the lamp light was focused onto the back pupil of the objective to illuminate the  
413 sample area using a 100X, 0.75 NA objective. The excitation power of the white light was  
414 maintained at approximately 100 nW. The reflected light was collected by the same objective, and  
415 a dual-axis galvo mirror scanning system was employed. Following the spatial scanning of the  
416 sample, controlled by the angles of the galvo mirrors, the reflected light was spatially filtered  
417 through a pinhole and then dispersed by a spectrometer onto an InGaAs array (PyLoN-IR,  
418 Princeton Instruments).

#### 419 **Pump-probe measurements**

420 We carry out pump-probe experiments using femtosecond pulses (400 kHz, 1050 nm, 250 fs)  
421 generated by a solid-state laser (Light Conversion, Carbide). The laser output is split into two  
422 beams to form the pump and probe arms. For the probe, a portion of the fundamental beam is  
423 focused into a YAG crystal to generate a stable white light continuum, which is then spectrally  
424 filtered (1125 nm, 50 nm band-pass filter) to cover the exciton and trion energies in MoTe<sub>2</sub>. The  
425 pump beam is directed to a motorized delay stage to control the pump-probe delay, Δt, and then  
426 focused onto a second YAG crystal to generate another broadband white light continuum, which  
427 is subsequently filtered down to 1250 ± 50 nm. After filtering, the pump beam passes through an  
428 optical chopper to generate alternating pump-on and pump-off signals. The pump and probe beams  
429 are then directed collinearly onto the sample through a 100X, 0.75 NA objective. The pump and

430 probe spot diameters are approximately 1.5  $\mu\text{m}$  and 1  $\mu\text{m}$ , respectively. The pulse duration at the  
431 sample was estimated to be  $\sim 200$  fs from the coherent artifact in pump-probe cross correlation.  
432 The same objective is used to collect the reflected light, which is spectrally filtered to remove the  
433 pump component and then dispersed onto an InGaAs detector array (PyLoN-IR, Princeton  
434 Instruments). The pump-on and pump-off spectra at varying  $\Delta t$  are used to calculate the transient  
435 reflectance signal ( $\Delta R/R$ ), where  $\Delta R = R(\Delta T) - R$  and  $R$  is reflectance without pump. For the  
436 linecuts in Figure 1g and Figure 2d, we integrate in small probe photon energy windows as shown  
437 by dashed boxes on the 2D spectral maps in Extended Data Figure 9. Note that, at the pump photon  
438 energy used here, there is no detectable excitation directly of the semiconducting MoTe<sub>2</sub>. Such  
439 excitation would lead to Pauli blocking which would give rise to a nearly instantaneous bleaching  
440 signal at exciton/trion energies; this was not observe in time-resolved spectra. We use excitation  
441 photon energy below the optical gap of MoTe<sub>2</sub> to avoid the creation of excitons; pump excitation  
442 above the optical gap would result in overwhelming response of bleaching and recombination  
443 dynamics of excitons/trions. In the measurement, we vary the pump fluence from  $\rho = 7$  to 42  
444  $\mu\text{J}/\text{cm}^2$ , use a probe fluence of 22  $\mu\text{J}/\text{cm}^2$  for all the measurement, Extended data fig. 10. The peak  
445 amplitude of  $\Delta R/R$  signal is found to scale linearly with pump fluence. The electronic melting and  
446 recovery dynamics are independent of  $\rho$  in this range. In all data presented in the text, we use  
447 constant pump and probe fluences of 42  $\mu\text{J}/\text{cm}^2$  and of 22  $\mu\text{J}/\text{cm}^2$ , respectively.

#### 448 **Coherent phonons launched at graphite electrodes**

449 The few-layer graphene/graphite gate electrodes in a vdW structure are known to function as  
450 opto-elastic transducers<sup>36,37</sup>. Since the density of electrons that can be excited by the pump photon  
451 of  $\hbar\omega = 0.99$  eV is approximately three orders of magnitude higher in the graphite electrode than  
452 that in the doped moiré structure, most of the absorption of pump light occurs in the former. The  
453 resulting strain field in the photo-excited graphite electrodes launch acoustic phonon wavepackets  
454 that propagate through the h-BN spacer and reach the tMoTe<sub>2</sub> at a time delay determined by the  
455 spacer thickness and the phonon group velocity. We estimate that phonon group velocity from the  
456 arrival time of the wavepackets and the h-BN thickness:  $v_{ph}^g \approx d_{hBN}/t_{delay} \approx 3.5$  km/s, in agreement  
457 with the longitudinal acoustic phonon velocity in h-BN<sup>37</sup>. The phonon wavepackets modulate the  
458 electronic structure and the effective dielectric environment of tMoTe<sub>2</sub>, enabling detection of the  
459 phonon oscillations through coherent changes in the exciton resonances in MoTe<sub>2</sub>. The acoustic

460 phonon wavepackets launched from the graphite electrodes are broad band and those detected at  
461 tMoTe<sub>2</sub> are frequency selected by resonant modes, particularly inter-layer breathing (LB) mode in  
462 the multilayer vdW structure<sup>36,37</sup>.

463 Excitation of hot electrons/holes in the few-layer graphene electrode is also responsible for the  
464 initial spike in the  $\Delta R/R$  signal, with a main decay channel at  $\Delta t \leq 1$  ps<sup>16,17</sup>. At the excitation  
465 fluences used here, the optical response of the few-layer graphene electrode is dominated by pump-  
466 induced bleaching of inter-band transition<sup>43</sup> and the cooling of hot carriers in the electrode is likely  
467 responsible for the decaying background tail, which is most obvious in the absence of electronic  
468 melting at  $v = 0$  (Fig. 4d).

469 **Assignment of Filling Factors**

470 The filling factor  $v$  is defined as the number of electrons or holes per moiré superlattice site.  
471 To determine  $v$ , we use the well-established insulating states,  $v = 0$ ,  $v = \pm 1$  and  $v = \pm 2$  as reference  
472 points to extract the conversion factor between gate voltage ( $V_g = V_{tg} + V_{bg}$ ) and the filling factor  
473 for both electron and hole doping. We start by identifying the gate voltages for all insulating states,  
474 determined by the maximum change in reflection observed in the pump-probe map (e.g., Fig. 1g).  
475 For distinct and closely spaced states, we determine their peak positions and full width at half-  
476 maximum (FWHM) by fitting Lorentzian profiles to the exciton/trion spectral weight as a function  
477 of gate voltage. To reduce interference effects from the top and bottom hBN layers and the  
478 substrate, which can distort the reflection spectrum, we integrate the reflection contrast over an  
479 energy window around the exciton/trion peak to extract the spectral weight (see Extended Data  
480 Fig. 9). The fitting results for all states, along with the corresponding gate voltages, are presented  
481 in Extended Data Table 1.

482 For device D1, the gate voltages corresponding to  $v = 0$ ,  $v = 1$  and  $v = -1$  are determined from  
483 the static and transient reflection. Using a linear fit to these points, we establish the relationship  
484 between filling factor and gate voltage. The filling factors for other insulating states are then  
485 calculated based on their gate voltages and the conversion factor. Each state is assigned to the  
486 closest rational number with a small denominator, as these generally represent lower-energy states.

487 For device D2, we applied the same method to determine the states between  $v = 1$  and  $v = -1$ .  
488 Two peaks close to  $v = 0$  ( $|v| < 1/7$ ), were not assigned specific filling factors due to the limited  
489 resolution and uncertainty in the precise gate voltage at  $v = 0$ . For states  $|v| > 1$ , the gate voltage

490 becomes more effective; therefore, we used  $v = -2$ ,  $v = -1$  and  $v = 0$  to define the relationship for  $-$   
491  $2 < v < -1$  states and use  $v = 0$ ,  $v = 1$  and  $v = 2$  to define the relationship for  $v > 1$ . For less well-  
492 developed states ( $v < -2$ ), we estimated the peak positions and widths from the first derivative of  
493 the reflection contrast contour plot with respect to energy (see Fig. 2c and d for the averaged  
494 derivative map at different time delays, and Extended Data Fig. 4 for individual time delays). The  
495 gate voltages corresponding to these correlated states are determined by the inflection points in the  
496 derivative map and the associated spectral weight.

497

## 498 References

- 499 43. Malard, L. M., Mak, K. F., Neto, A. H. C., Peres, N. M. R. & Heinz, T. F. Observation of  
500 intra-and inter-band transitions in the transient optical response of graphene. *New J Phys*  
501 **15**, 015009 (2013).

502

## 503 ACKNOWLEDGEMENTS

504 This research, including all time-resolved spectroscopy experiments presented in the main text,  
505 was primarily supported by Programmable Quantum Materials, an Energy Frontier Research  
506 Center funded by the U.S. Department of Energy (DOE), Office of Science, Basic Energy Sciences  
507 (BES), under award DE-SC0019443. Additional support came from DOE-BES under award  
508 number DE-SC0024343 (XYZ) for pump-probe methodology development, DOE-BES under the  
509 award DE-SC0018171(XX) for device fabrication, US Army Research Office grant number  
510 W911NF-23-1-0056 (XYZ and XR) for the temperature-dependent experiments, Department of  
511 Defense Multidisciplinary University Research Initiative (XYZ) grant number W911NF2410292  
512 for the development of mechanistic models of electron-phonon coupling, and Materials Science  
513 and Engineering Research Center through NSF grant DMR-2011738 for facilities used in sample  
514 characterizations. YW acknowledges the Max-Planck New York Center (MPNYC) for fellowship  
515 support. EAA acknowledges support from the Simons Foundation as a Junior Fellow in the Simons  
516 Society of Fellows (965526). K.W. and T.T. acknowledge support from the JSPS KAKENHI  
517 (Grant Numbers 21H05233 and 23H02052) and World Premier International Research Center  
518 Initiative (WPI), MEXT, Japan. We thank Nishchhal Verma and Daniel Munoz Segovia for helpful  
519 discussions, Yinjie Guo, Jordan Pack, and Sanat Ghosh for assistance with sample preparation.

## 520 Author Contributions

Y.W., X.Y.Z., and X.X. conceived this work. Y.W., along with J.C., conducted all spectroscopic measurements, analyzed, and interpreted the results, with the assistance of E.A.A. and YL, and inputs from D.B., X.R., and J.C.H. E.A. was responsible for the fabrication and characterization of sample (D1) and W.L. for sample (D2), under the supervision of X.X. T.T. and K.W. provided the hBN crystal. J.I., R.Q., X.H., and D.X. contributed to mechanistic interpretations. The manuscript was prepared by Y.W. and X.Y.Z., incorporating inputs from all coauthors. X.Y.Z. supervised the project. All authors read and commented on the manuscript.

**Competing Interests.** The authors declare no competing interests.

**Data Availability Statement.** The data shown in the main figures are available in Source Data. Data supporting the findings of this study are available from the corresponding author upon request.

**Extended Data Fig. 1: Device Images and characterization.** **a-b.** 50X microscope image of device D1 and D2, the scale bar is 20  $\mu\text{m}$ . **c.** RMCD signal versus  $v$  and perpendicular electric field  $D$  at zero magnetic field  $\mu_0H = 0$  (D1). The phase space with non-vanishing signal corresponds to the ferromagnetic state. **d.** RMCD signal versus vertical magnetic field with  $\mu_0H$  swept back and forth at  $n = -0.4 \times 10^{13} \text{ cm}^{-2}$  and  $D = 0 \text{ V/nm}$  (D2). **e.** D1: PL intensity plot as a function of doping and photon energy. **f.** D2: PL intensity plot as a function of doping and photon energy. **g.** Reflection as a function of doping and photon energy (D1). **h.** Reflection as a function of doping and photon energy (D2).

**Extended Data Fig. 2: Pump-probe spectroscopy at T = 7, 20, 50 K of tMoTe<sub>2</sub> device 1 (D1) with a twist angle  $\theta = 3.7^\circ$ .** Transient reflection spectrum as a function of carrier density ( $n$ ) and probe photon energy  $E(\hbar\omega_2)$  at pump-probe delays of **a-d.**  $\Delta t = 4 \text{ ps}, 39 \text{ ps}, 399 \text{ ps}$  and  $1399 \text{ ps}$  at 7K. **e-h.**  $\Delta t = 4 \text{ ps}, 39 \text{ ps}, 399 \text{ ps}$  and  $1399 \text{ ps}$  at 20K. **i-l.**  $\Delta t = 4 \text{ ps}, 39 \text{ ps}, 399 \text{ ps}$  and  $1399 \text{ ps}$  at 50K. All measurements were conducted at a pump fluence of  $54 \text{ uJ/cm}^2$  with the transient reflection range  $\Delta R/R_0$  from  $-2 \times 10^{-4}$  to  $2 \times 10^{-4}$ . There is no external magnetic field ( $B = 0$ ) or displacement field ( $D = 0$ ).

**Extended Data Fig. 3: Pump-probe spectroscopy of a tMoTe<sub>2</sub> device (D3) with a twist angle  $\theta = 5.5^\circ$ .** **a.** Optical image ( $\sim 100 \mu\text{m} \times 100 \mu\text{m}$ ) of device D3. **b.** PL spectra as a function doping level (estimated from calculated capacitance). The left and right show displacements fields of  $D = 0$  and  $-0.02 \text{ V/nm}$ ; the latter is used to compensate for a small build-in potential; **c-e** Transient reflection spectrum as a function of total gate voltage  $V_g$  (V) and probe photon energy  $E(\hbar\omega_2)$  at pump-probe delays of **c.**  $\Delta t = 7 \text{ ps}$ , **d.**  $\Delta t = 13 \text{ ps}$ , and **e**  $\Delta t = 500 \text{ ps}$ . The pump ( $0.99 \text{ eV}$ ) and probe fluences are at  $42 \text{ uJ/cm}^2$  and  $22 \text{ uJ/cm}^2$ , respectively. Sample temperature  $T = 1.6 \text{ K}$ . There is no external magnetic field ( $B = 0$ ) or displacement field ( $D = 0$ ). The gate voltage ranges in **c-e** correspond to the same estimated doping range shown in the PL maps **b.**

558 No specific states (at particular  $V_g$  or doping levels) are resolved in the pump-probe spectral maps  
559 at all three selected  $\Delta t$  values (7, 13, 500 ps), in agreement with the PL maps in **b**. The transient  
560 spectral maps feature exciton and trion resonances, with energy splitting in certain doping ranges;  
561 these splitting features have been observed before and attributed to exciton/trion fine structures in  
562 MoTe<sub>2</sub> monolayers (*Nature Nanotech.* **2013**, *9*, 634-638; *Nature Nanotech.* **2017**, *12*, 144-149)  
563 and/or exciton polarons in tMoTe<sub>2</sub> bilayers (*Nature Nanotech.* **2022**, *17*, 934-939). The broad  
564 contrasts in exciton/trion  $\Delta R/R$  signal vary slowly with  $\Delta t$  and likely result from the dynamics or  
565 hot-carrier relaxation, carrier-phonon scattering, phonon cooling, and balances in exciton and trion  
566 populations.

567 **Extended Data Fig. 4: Melting dynamics of correlated states.** **a.** Transient reflection spectra at  
568 the indicated pump-probe delay times (from top to bottom) of  $\Delta t = 1.5, 13, 25, 37, 49, 150, 450$   
569 and 1150 ps for **a.** hole doping and **b.** The corresponding 1<sup>st</sup> derivative (with respect to n) of the  
570 transient reflection spectra in **a.** All spectra obtained from tMoTe<sub>2</sub> device D2 ( $\theta = 3.1^\circ$ ), at a  
571 temperature of  $T = 2$  K, with no external electric or magnetic field.  
572

573 **Extended Data Fig. 5: Time profiles of difference states.** **a.** Time profiles of all the electron  
574 doping states in D1. **b.** electronic meting and recovery time constant of all the electron doped  
575 states. **c.** phonon melting and recovery time constant of electron doped states **d.** Time profiles of  
576 hole doped states. **e.** electronic meting and recovery time constant of all the hole doped states. **f**  
577 Time profile of  $v = 0, 1/3$  and  $1/2$ , data normalized to  $t = 0$  ps. **g** Time profile difference of  $v =$   
578  $1/3, 1/2$  to  $v = 0$ . All data obtained at a temperature of  $T = 2$  K, with no external electric or magnetic  
579 field.  
580

581 **Extended Data Fig. 6: Time profiles of a hole doped state of  $-1/7 \leq v < 0$ , which is closest to**  
582  **$V_g = 0$ .** Upper: sample temperature  $T = 2$  K (nominal reading on sample stage 1.58 K); Lower:  
583 sample temperature  $T = 70$  K, which is above the  $T_c$ . Electronic and phonon melting processes are  
584 observed at 2 K, but not 70 K.  
585

586 **Extended Data Fig. 7: Delayed arrival of coherent phonon wavepackets launched at the**  
587 **graphite electrodes.** **a.** Time profiles of the  $v = 1$  state with melting and recovery fitting (red). **b.**  
588 coherent phonon oscillation after the melting and recovery background is subtracted. **c.** Fourier  
589 transform of the coherent phonons.  
590

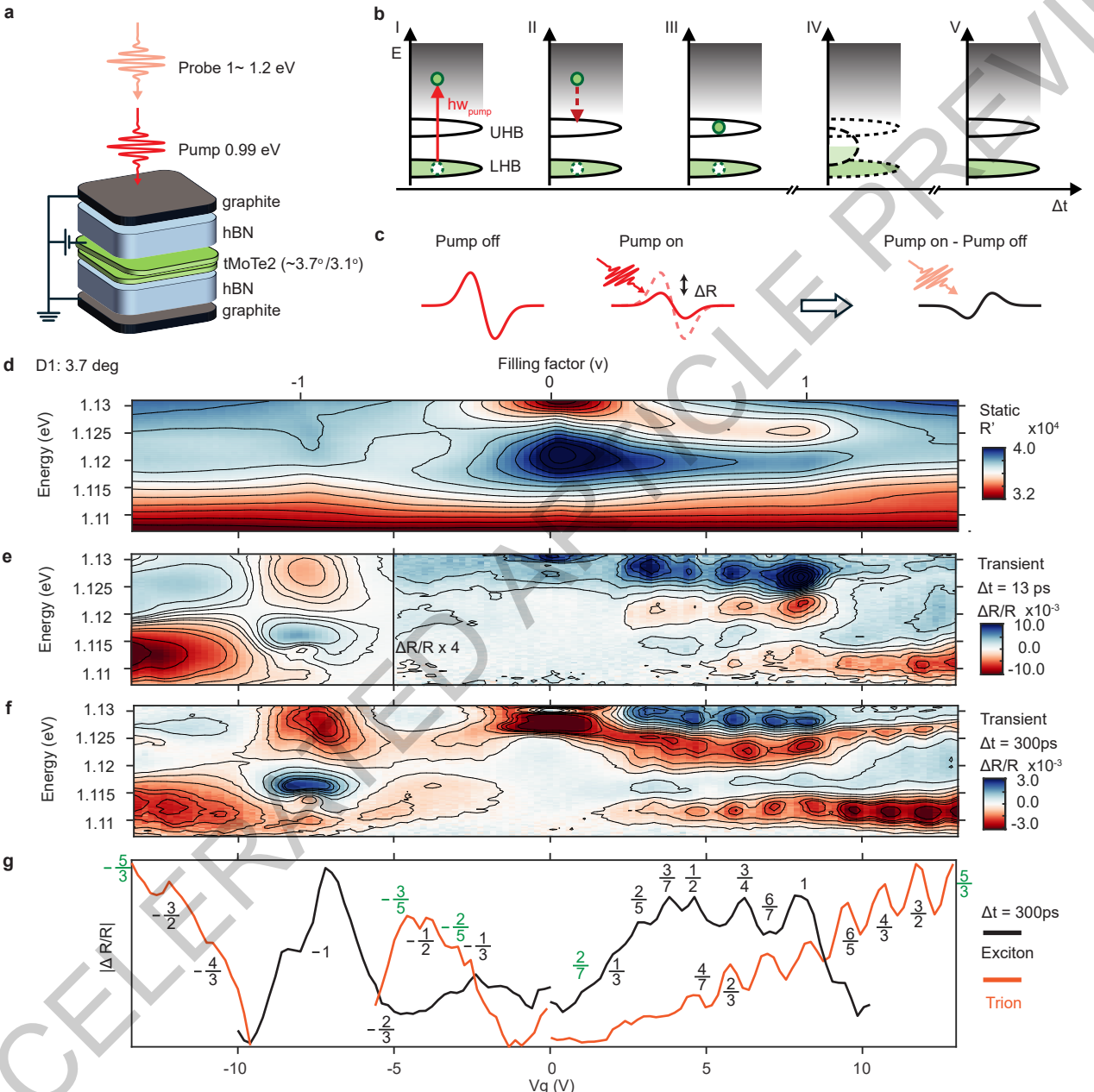
591 **Extended Data Fig. 8: spectral resolved time profile.** **a.** Transient reflection as a function of  
592 delay time and spectral energy for non-correlated state  $v = 0$  in D1. **b.** Short time window of **a.** **c.**  
593 Time profiles of the  $v = 0$  state at the exciton energy, only phonon modulation process observed.  
594 **d.** Transient reflection as a function of delay time and spectral energy for  $v = 1$  and **e.**  $v = -1$   
595

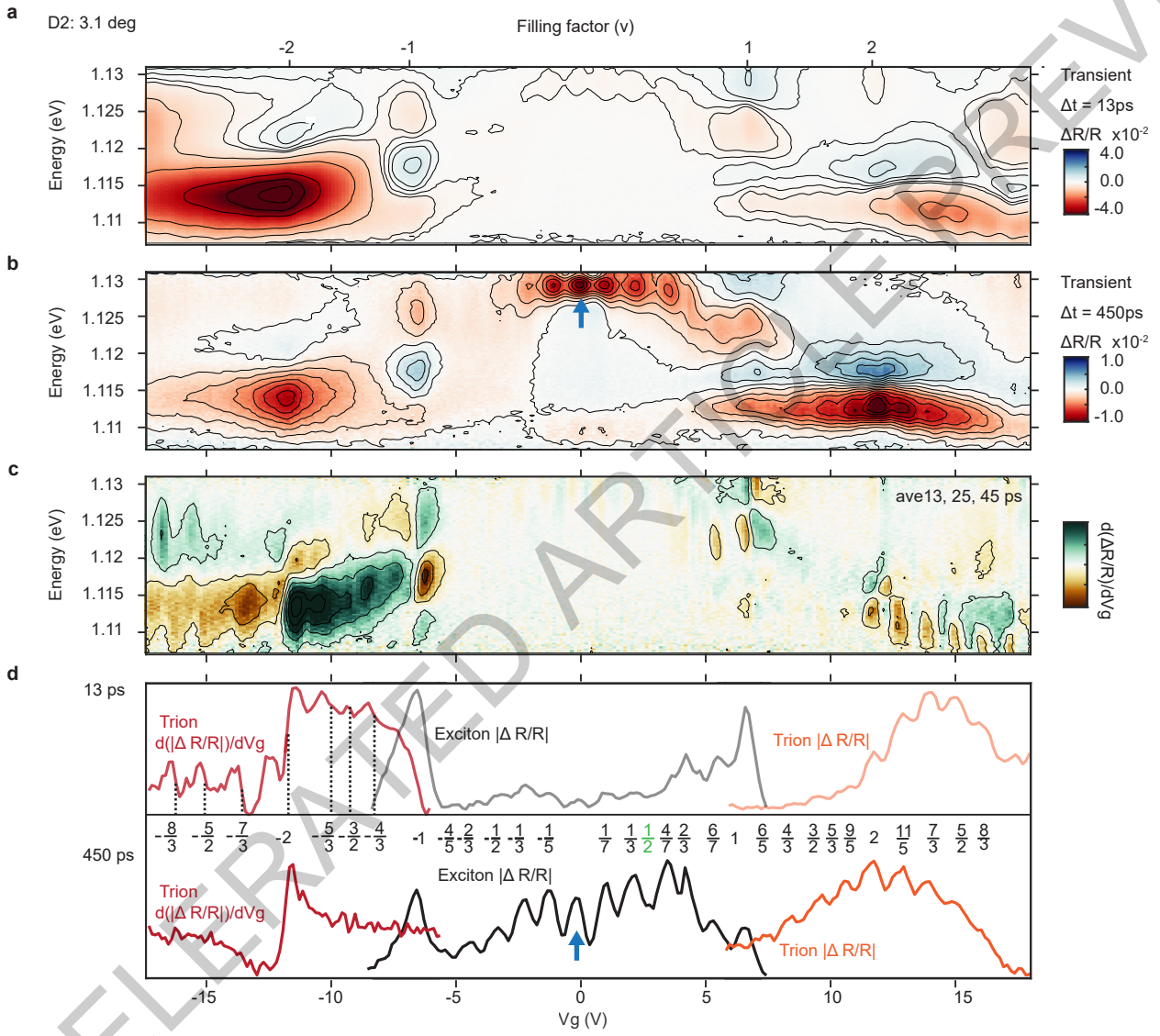
596 **Extended Data Fig. 9: Pump-probe spectroscopy at  $T = 2$  K of tMoTe<sub>2</sub>.** Transient reflection  
597 spectrum as a function of carrier density (n) and probe photon energy E ( $\hbar\omega_2$ ) at pump-probe delays  
598 of **a.** Device D1  $\Delta t = 300$  ps, with the dash line square indicating the integration range for the  
599 exciton (black) and trion (blue) shown in Figure 1g of the main text. **b.** Device D2  $\Delta t = 450$  ps,  
600 with the dash line square indicating the integration range for the exciton (black), trion (blue), and  
601 trion derivative (red) shown in Fig. 2d of the main text; trion D2 : 1.107—1.114 eV, exciton: 1.130  
602 1.122 eV, derivative: 1.115—1.106 eV device 1: trion electron doping 1.108-1.114 eV exciton

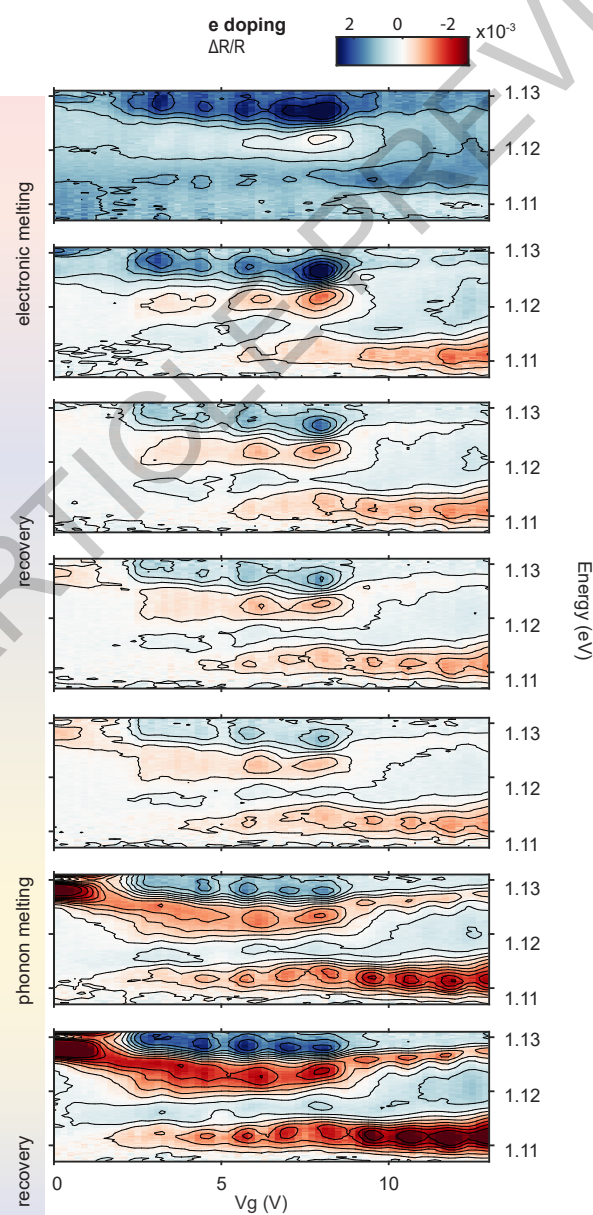
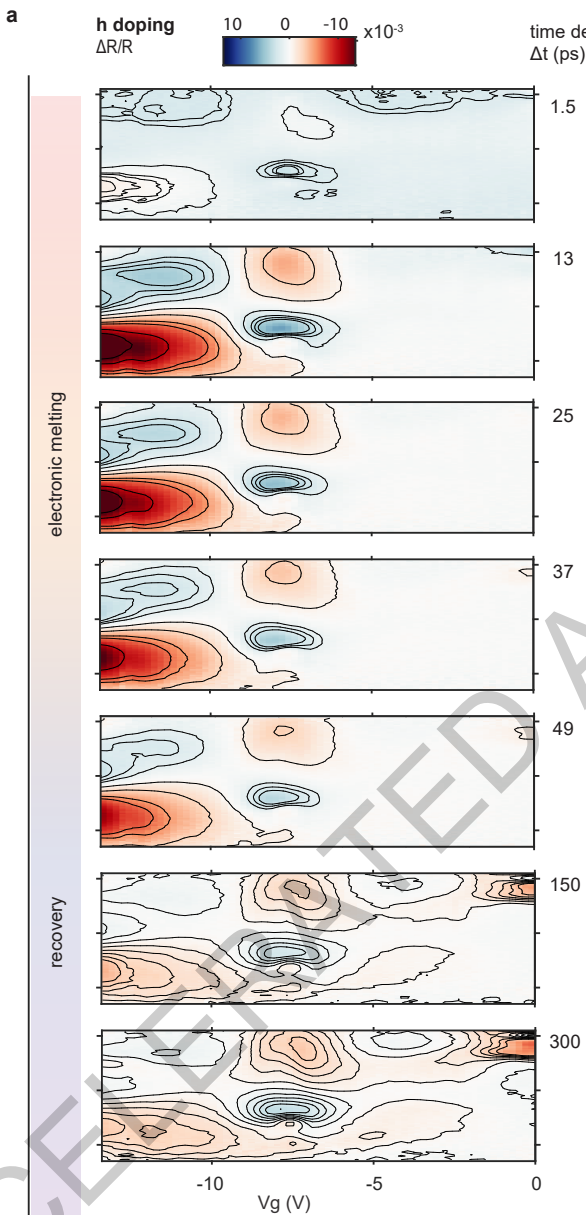
603 electron doping 1.120-1.125 eV, exciton hole doping 1.126-1.123 eV , trion hole doping: 1.112-  
604 1.117eV

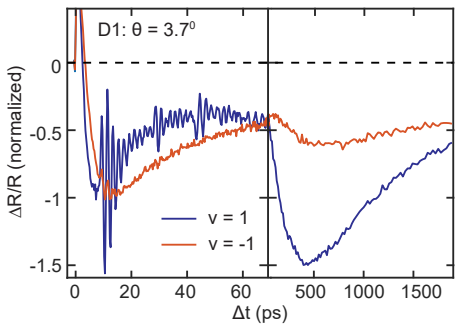
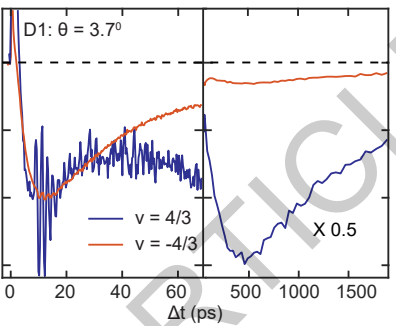
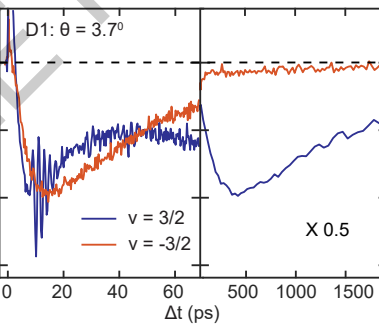
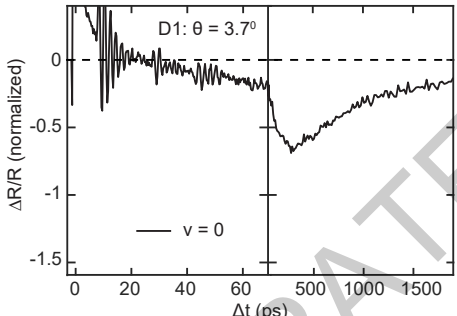
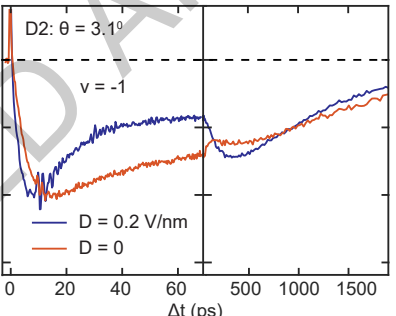
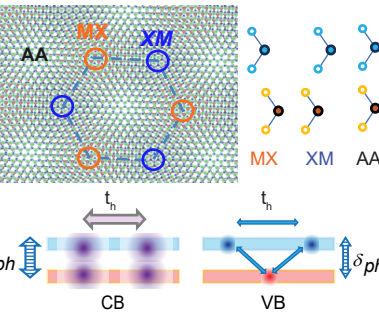
605  
606 **Extended Data Fig. 10: Pump fluence dependent.** **a** Transient reflection in the exciton spectral  
607 region for the  $v = 1$  state at pump fluences of  $\rho = 7, 14$ , and  $42 \mu\text{J}/\text{cm}^2$  and a pump-probe delay  
608 time of  $\Delta t = 7$  ps. The magnitude of  $\Delta R/R$  scales approximately linearly with  $\rho$ . Time profiles of  
609 the  $v = 1$  state at different fluences on two time scales **b** 0-75 ps and **c** 75-1875 ps. Each profile is  
610 obtained from integration of  $\Delta R/R$  in a probe photon energy window of 1.119-1.125 eV. All  
611 profiles in **b** and **c** are normalized to  $\Delta R/R$  at  $\Delta t = 7$  ps. The electronic melting/recovery processes  
612 are independent of  $\rho$  **b**, while the relative magnitude of the phonon melting processes increases  
613 with pump fluence **c**.

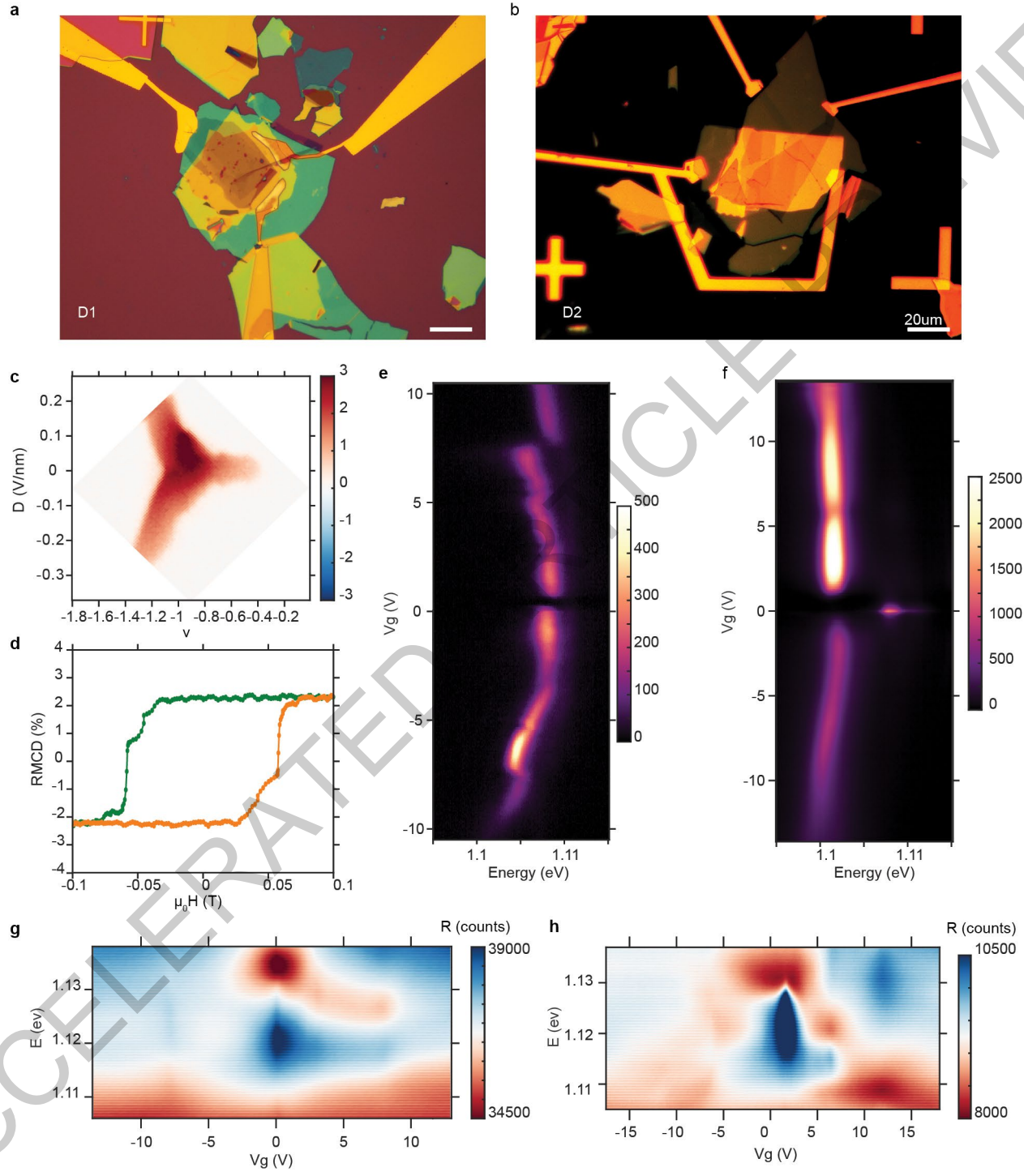
614  
615 **Extended Data Table. 1:** Filling factor assignment:



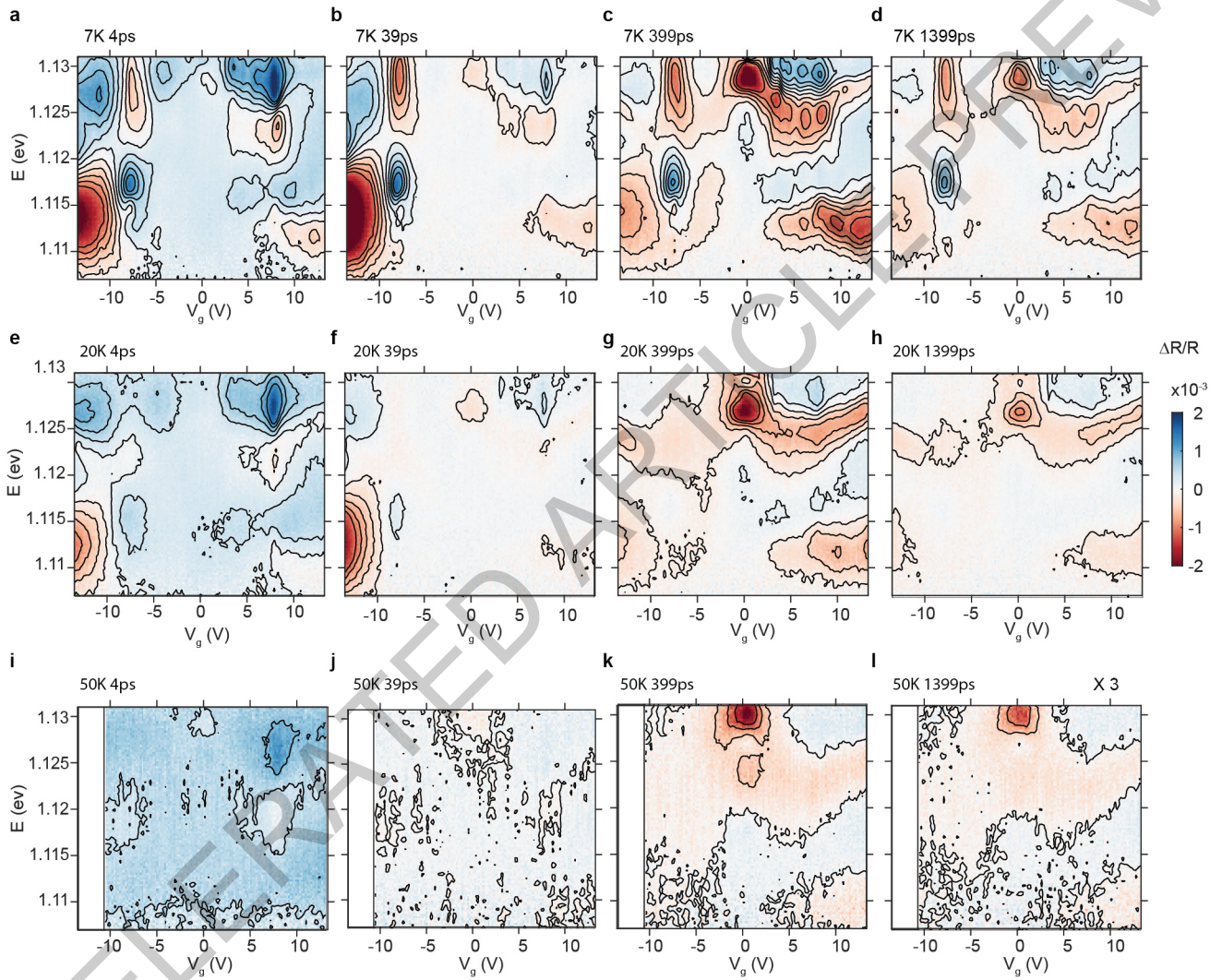




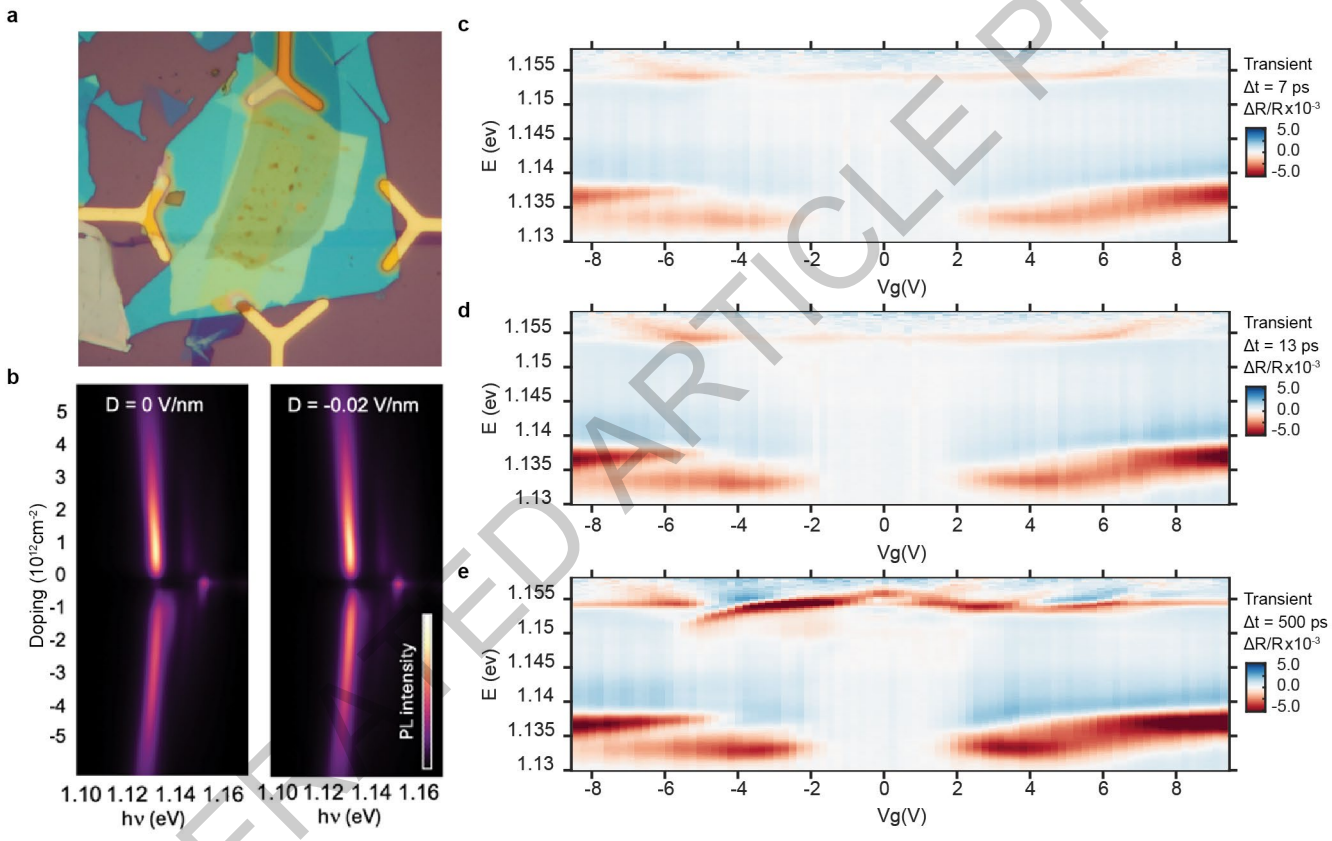
**a****b****c****d****e****f**



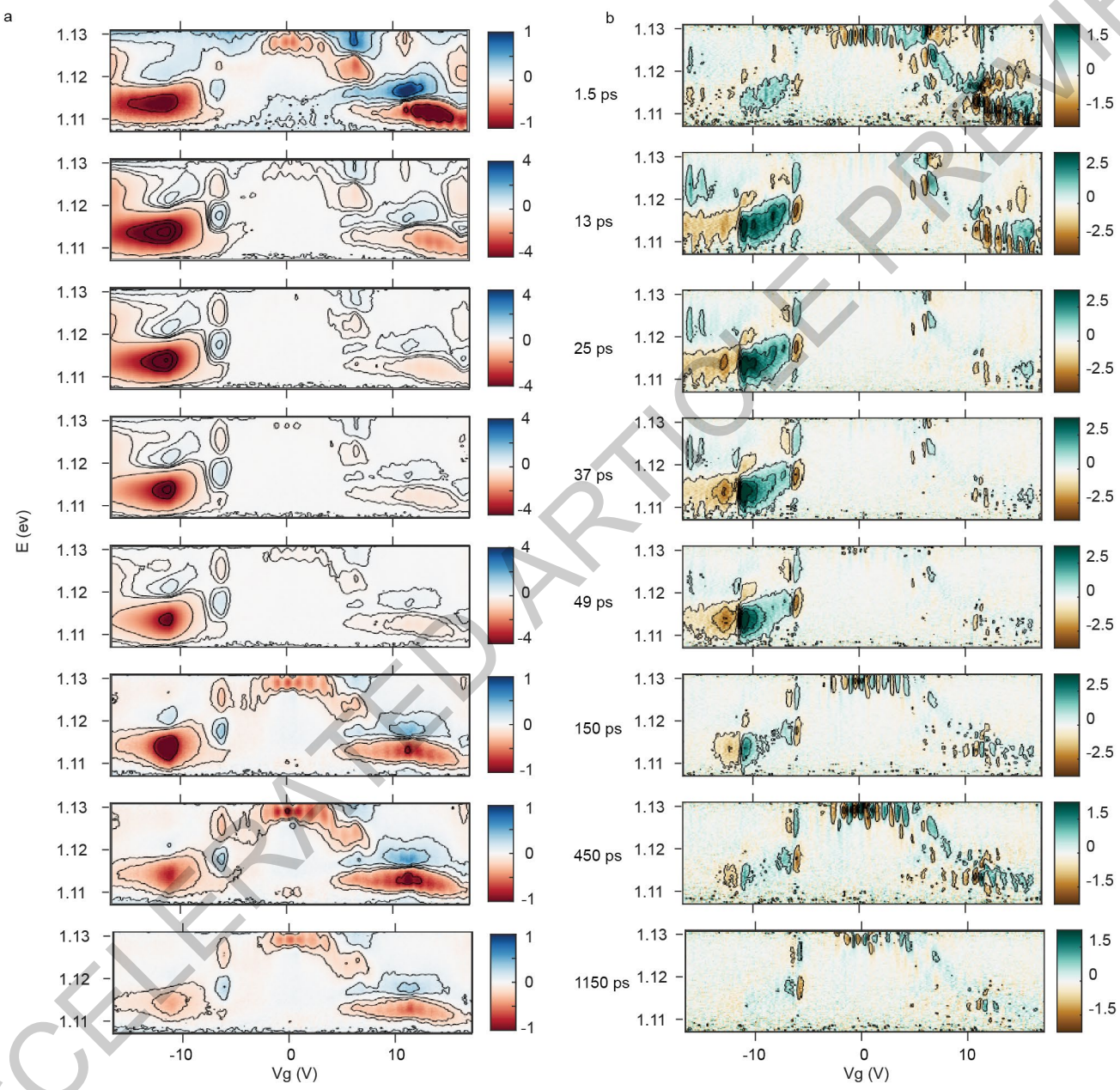
**Extended Data Fig. 1**



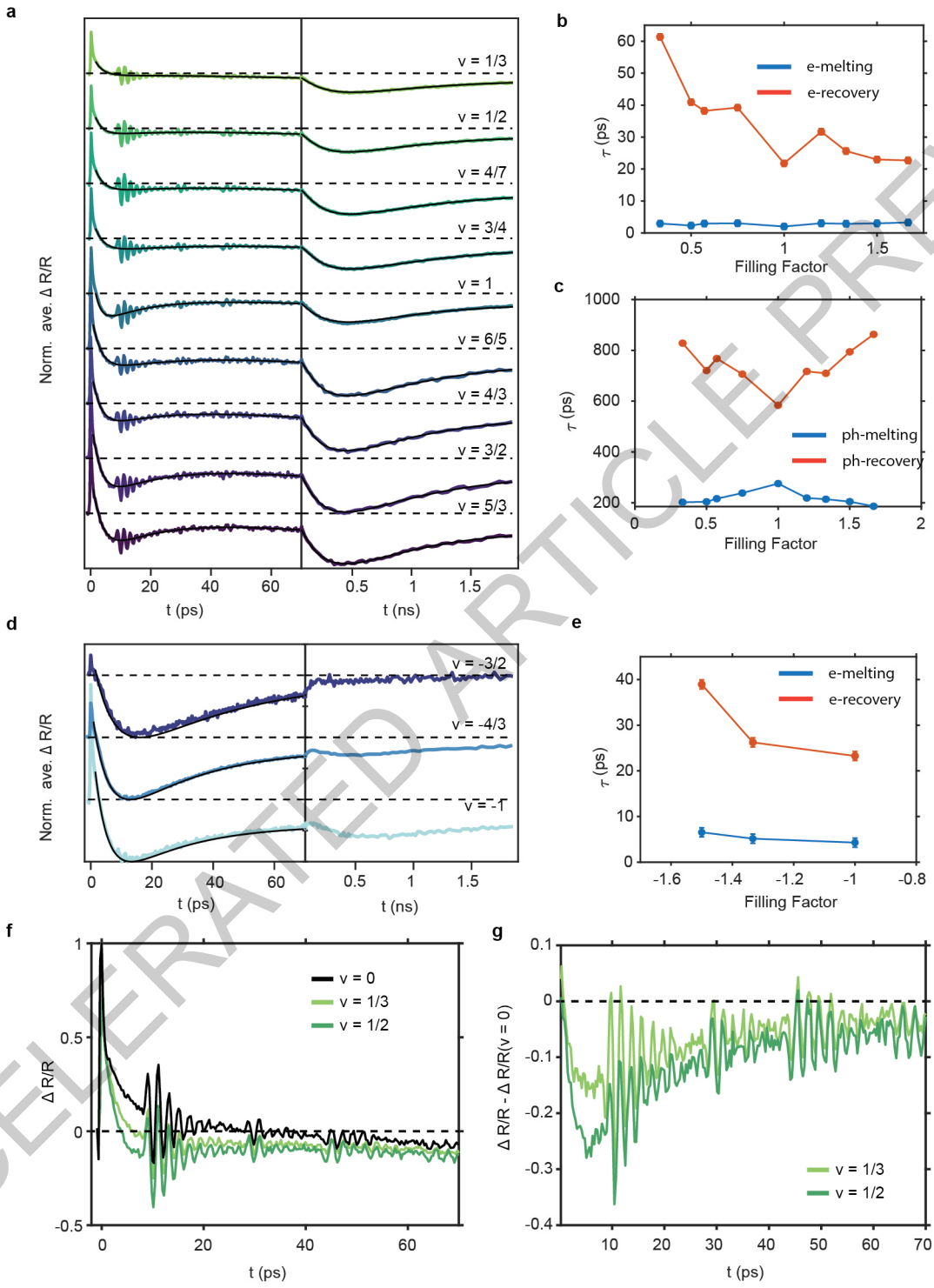
**Extended Data Fig. 2**



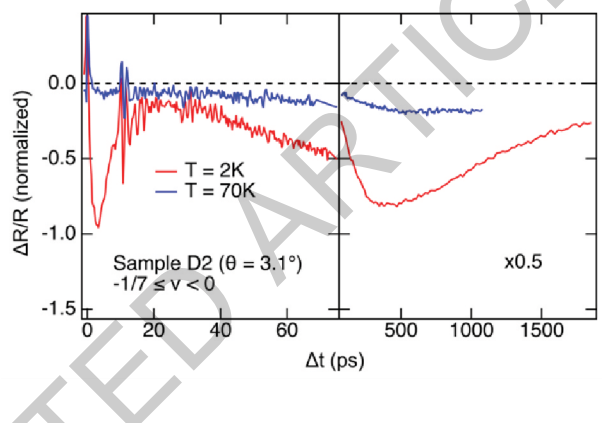
**Extended Data Fig. 3**



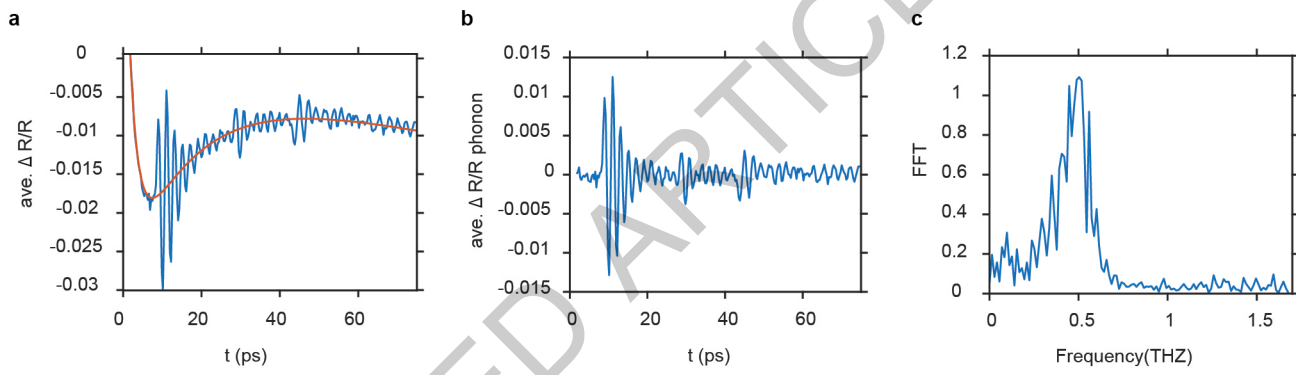
**Extended Data Fig. 4**



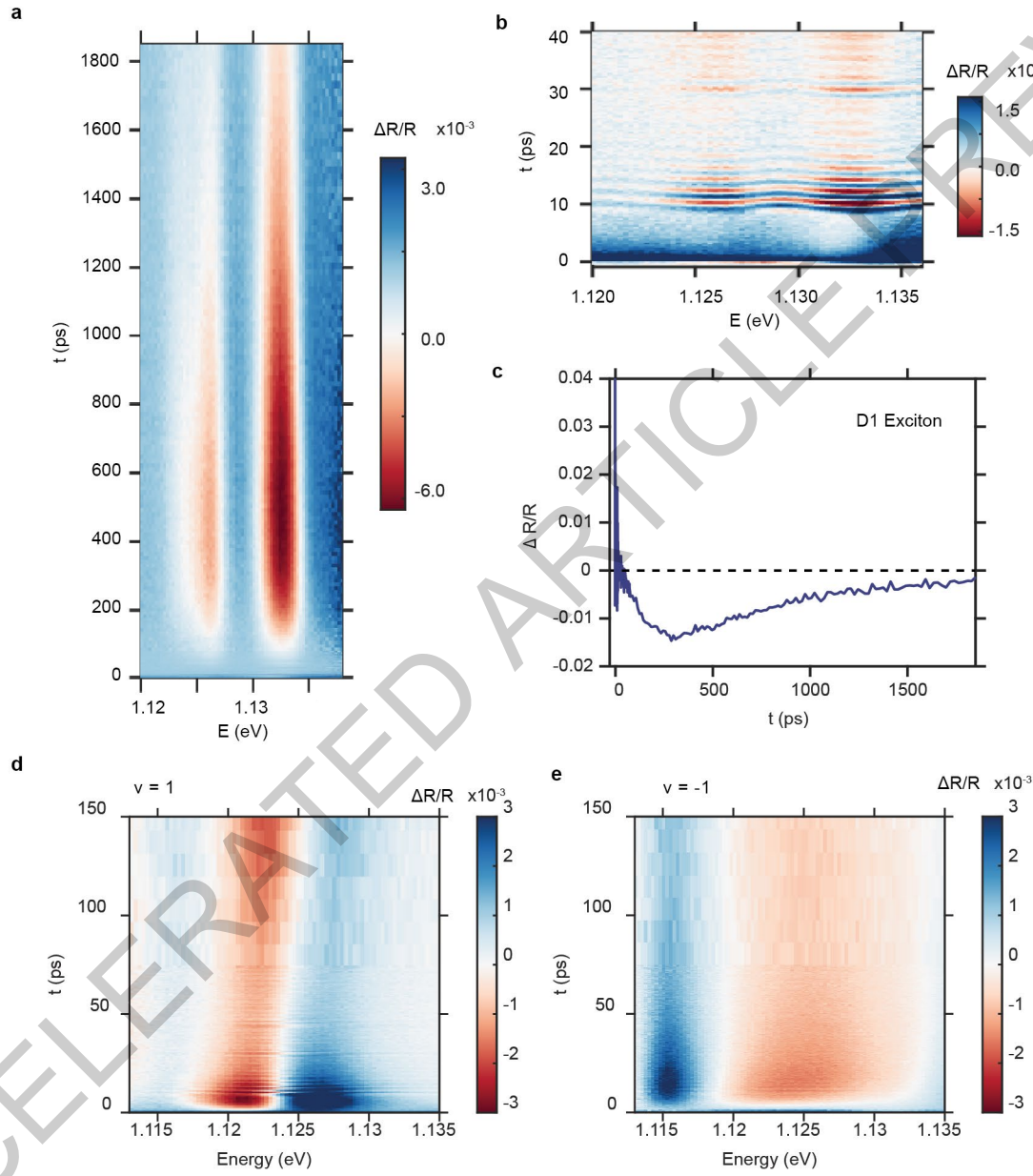
Extended Data Fig. 5



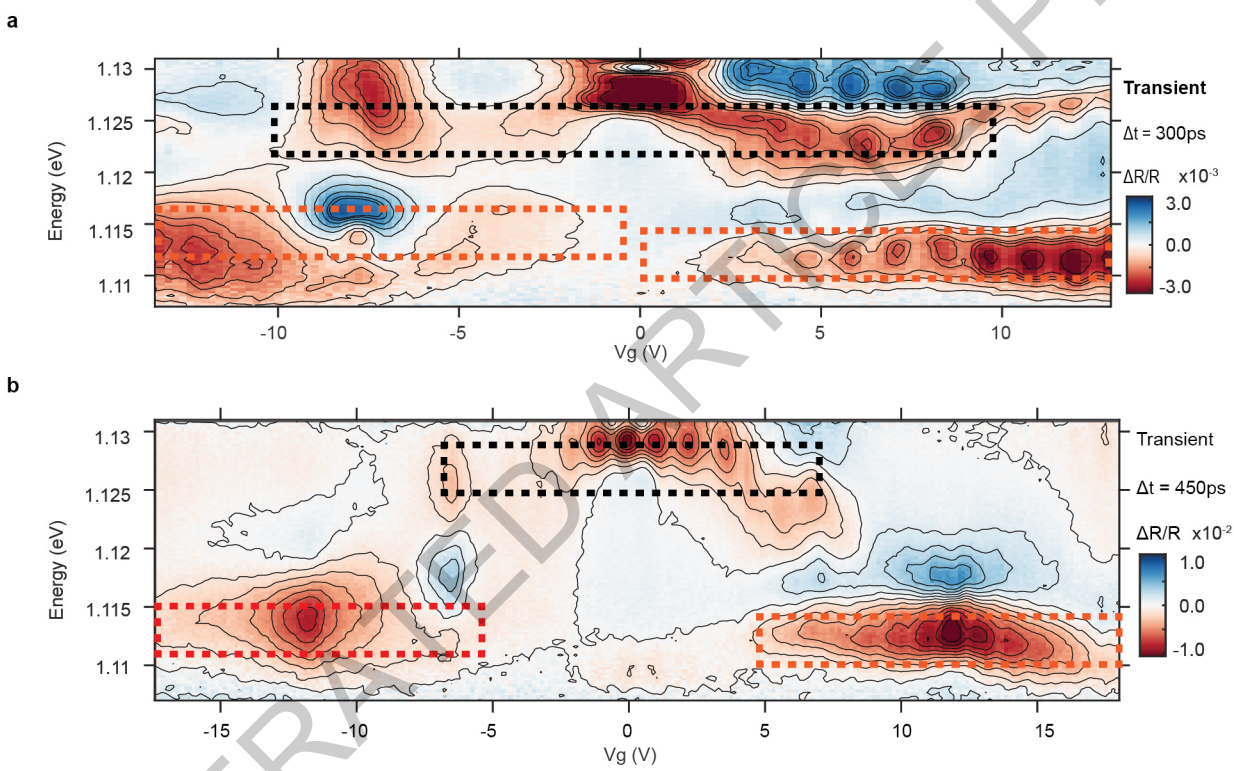
Extended Data Fig. 6



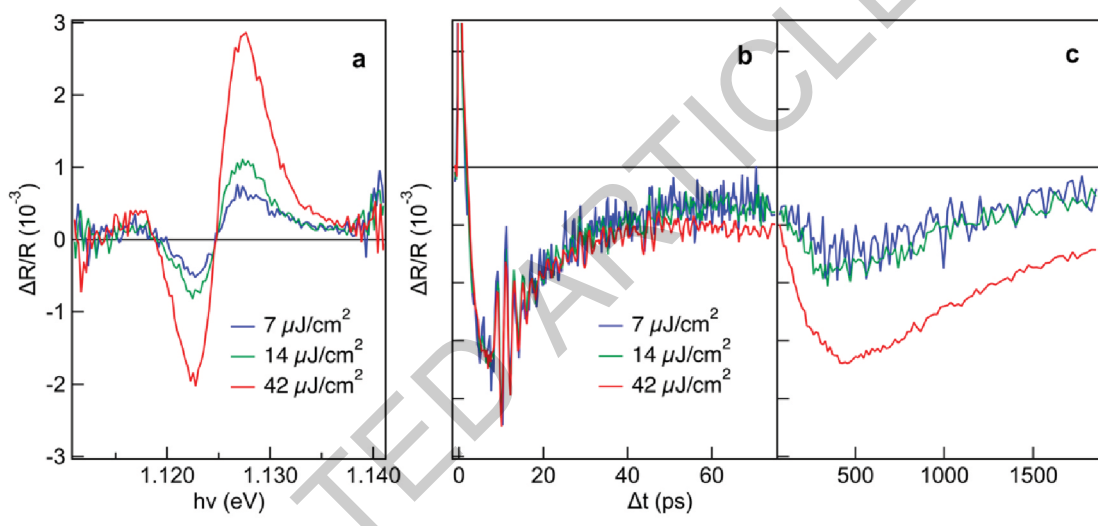
Extended Data Fig. 7



**Extended Data Fig. 8**



Extended Data Fig. 9



Extended Data Fig. 10

Extended table

Filling factor assignment:

D1			D2		
Filling factor (closest state)	Filling factor	Gate Voltage	Filling factor (closest state)	Filling factor	Gate Voltage
-5/3	-1.779	-13.600	-8/3	-2.702	-16.295
-3/2	-1.589	-12.150	-5/2	-2.500	-15.095
-4/3	-1.350	-10.325	-7/3	-2.239	-13.540
-1	-1	-7.644	-2	-1.967	-11.918
-2/3	-0.663	-5.069	-5/3	-1.636	-9.940
-3/5	-0.568	-4.344	-3/2	-1.493	-9.090
-1/2	-0.501	-3.834	-4/3	-1.327	-8.100
-2/5	-0.402	-3.079	-1	-1	-6.511
-1/3	-0.316	-2.418	-4/5	-0.802	-5.242
2/7	0.280	2.243	-2/3	-0.664	-4.336
1/3	0.345	2.756	-1/2	-0.497	-3.235
2/5	0.404	3.234	-1/3	-0.334	-2.157
3/7	0.469	3.758	-1/7	-0.163	-1.032
1/2	0.478	3.820	0	0	-0.028
4/7	0.578	4.622	1/7	0.155	1.063
2/3	0.729	5.836	1/3	0.327	2.198
3/4	0.732	5.856	4/7	0.541	3.608
6/7	0.879	7.033	2/3	0.661	4.402
1	1	8.000	6/7	0.829	5.510
6/5	1.190	9.522	1	1	6.672
4/3	1.331	10.645	6/5	1.163	7.709
3/2	1.493	11.943	4/3	1.333	8.830
5/3	1.625	13.000	3/2	1.506	9.970
			5/3	1.633	10.808
			9/5	1.764	11.675
			2	1.990	11.940
			11/5	2.182	13.070
			7/3	2.349	14.060
			5/2	2.494	14.910
			8/3	2.684	16.030

Extended Data Table 1